The sapphirine-bearing rocks in contact with the Lherz peridotite body: new mineralogical data, age and attempt at interpretation

Jessica Uzel, Yves Lagabrielle, Serge Fourcade, C. Chopin, P. Monjoux, C. Clerc, Marc Poujol

▶ **To cite this version:**

Jessica Uzel, Yves Lagabrielle, Serge Fourcade, C. Chopin, P. Monjoux, et al.. The sapphirine-bearing rocks in contact with the Lherz peridotite body: new mineralogical data, age and attempt at interpretation. Bulletin de la Société Géologique de France, 2020, 191, pp.5. 10.1051/bsgf/2019015 . insu-02390651v1

HAL Id: insu-02390651

https://insu.hal.science/insu-02390651v1

Submitted on 5 Dec 2019 (v1), last revised 20 Jan 2021 (v2)

HAL is a multi-disciplinary open access archive for the deposit and dissemination of scientific research documents, whether they are published or not. The documents may come from teaching and research institutions in France or abroad, or from public or private research centers.

L'archive ouverte pluridisciplinaire **HAL**, est destinée au dépôt et à la diffusion de documents scientifiques de niveau recherche, publiés ou non, émanant des établissements d'enseignement et de recherche français ou étrangers, des laboratoires publics ou privés.

Distributed under a Creative Commons Attribution 4.0 International License

Submitted to BSGF, October 23th 2019. Second revision version.

The sapphirine-bearing rocks in contact with the Lherz peridotite body: new mineralogical data, age and interpretation

Les roches à saphirine au contact du corps de péridotites de Lherz : nouvelles données minéralogiques, âge et nouvelle interprétation

Jessica Uzel[a*], Yves Lagabrielle[a], Serge Fourcade[a], Christian Chopin[b], Pierre Monchoux[c], Camille Clerc[d] and Marc Poujol[a]

[a]: Univ Rennes, CNRS, Géosciences Rennes, UMR 6118, 35000 Rennes, France

[b]: Laboratoire de Géologie de l'ENS, UMR 8538, ENS–CNRS, PSL Research University, 24 rue Lhomond, 75005 Paris, France

[c]: Université de Toulouse, CNRS, GET, IRD, OMP, 14 Av. Edouard Belin, Toulouse 31400, France

[d]: Laboratoire Insulaire du Vivant et de l'Environnement, Université de la Nouvelle Calédonie, BPR4, 98851 Nouméa Cedex, France

[*] Correspondence: jessica.uzel@univ-rennes1.fr

Declaration of interest: none.

Mots-clés : Zone nord-pyrénéenne ; Saphirine ; Keuper ; Méta-évaporite ; Métamorphisme de haute température et basse pression ; Exhumation du manteau ; Détachement extensif.

Keywords: North Pyrenean Zone; Sapphirine; Keuper; Meta-evaporite; High-temperature low-pressure metamorphism; Mantle exhumation; Extensional detachment.

Résumé

Des roches contenant de la saphirine ont été décrites dans le Bassin d'Aulus (Ariège, France), au sein d'une zone de contact entre le corps de péridotites de Lherz et les métasédiments mésozoïques affectés au Crétacé par un métamorphisme de haute température et de basse pression (Monchoux, 1970, 1972a, b). La saphirine se trouve dans des dépôts clastiques lités caractérisés par une association minérale rare, riche en Al et Mg. Nous présentons ici les résultats de l'étude pétrographique détaillée de seize échantillons représentatifs de la diversité des roches à saphirine de Lherz. Ces brèches et microbrèches sont constituées de clastes monominéraux et polyminéraux de composition variable. Les protolithes de certains de ces clastes sont aisément identifiables : roches ultramafiques, méta-ophites, « cornéennes micacées », socle paléozoïque. Néanmoins, une grande partie des roches à saphirine est composée de débris mono- et polyminéraux dont le ou les protolithes sont inconnus dans la région et restent à identifier. Ces protolithes énigmatiques sont nécessairement composés des minéraux de l'ensemble que nous appelons « assemblage minéralogique à saphirine » (sapphirine-bearing mineral suite : SBMS) et qui comprend les espèces suivantes : saphirine + enstatite + spinelle alumineux + Mg-amphiboles + Ca-amphiboles + kornérupine + minéraux accessoires (apatite, diopside, rutile, serpentine, smectite, tourmaline, vermiculite et mica blanc). Nous mettons en évidence la présence d'inclusions d'anhydrite et d'apatite riche en F, Cl et Sr dans les espèces minérales du SBMS, ainsi qu'une proportion dominante d'éléments clastiques issus du métamorphisme de roches du Keuper dans l'ensemble des échantillons étudiés. La texture bréchique ainsi que la présence de figures sédimentaires dans les roches à saphirine montrent que leur(s) protolithe(s) a (ont) été soumis à un processus de désagrégation mécanique suivi du vannage des clastes en milieu aqueux. Un faible mélange entre les différentes sources est établi par la composition lithologique des roches étudiées.

Une étude géochronologique par la méthode U-Pb sur rutile a été réalisée afin d'apporter des contraintes sur l'âge d'une (ou de la) source de ces dépôts clastiques. L'âge obtenu (98,6 ± 1,2 Ma) est interprété comme l'âge du métamorphisme de l'assemblage minéralogique à saphirine. Les roches à saphirine ont jusqu'à présent été interprétées comme du matériel crustal modifié en profondeur au contact des roches ultramafiques du corps de Lherz lors de leur remontée vers la surface. Les nouvelles contraintes géologiques apportées par cette étude impliquent : (i) l'origine triasique supérieure à jurassique inférieure du protolithe principal des roches à saphirine, (ii) le métamorphisme de ce protolithe en présence de saumures le long d'un détachement croûte-manteau actif et chaud au Cénomanien, et (iii) sa bréchification au cours de la remontée du matériel associée au fonctionnement du détachement, suivie du remaniement sédimentaire ultérieur de ce matériel métamorphique.

Abstract

Sapphirine-bearing rocks are described in the Aulus Basin (Ariège, France) in a contact zone between the Lherz peridotitic body and Mesozoic metasediments which underwent the Pyrenean Cretaceous high-temperature, low-pressure metamorphic event (Monchoux, 1970, 1972a, b). Sapphirine crystals occur in layered clastic deposits characterized by an uncommon suite of Al-Mg-rich minerals. A detailed petrographic study of sixteen samples representative of the diversity of the Lherz sapphirine-bearing rocks is presented.

These rocks include breccias and microbreccias with various compositions. Some samples are composed of polymineralic clasts and isolated minerals that derive from regionally well-known protoliths such as ultramafic rocks, meta-ophites, "micaceous hornfels", and very scarce Paleozoic basement rocks. Nevertheless, a large portion of the sapphirine-bearing clastic suite is composed of mono- and polymineralic debris that derive from unknown

protolith(s). We define a "sapphirine-bearing mineral suite" (SBMS) composed of monomineralic debris including: sapphirine + enstatite + aluminous spinel + Mg-amphiboles + Ca-amphiboles + kornerupine + accessory minerals (apatite, diopside, rutile, serpentine, smectite, tourmaline, vermiculite and a white mica). We highlight the dominance of metamorphic Keuper clastic materials in the studied rocks and the presence of inclusions of anhydrite and F-, Cl-, Sr-rich apatite in minerals of the Al-Mg-rich suite. The brecciated texture and the presence of unequivocal sedimentary features suggest that the sapphirine-bearing rocks were mechanically disaggregated and then experienced winnowing in underwater conditions with poor mixing between the different sources. We measured U-Pb rutile age data in order to provide constraints on the age of (one of) the protolith(s) of those clastic deposits. The obtained age (98.6 ± 1.2 Ma) is interpreted as the age of metamorphism of this protolith of the SBMS. Previous works interpreted the Lherz sapphirine-bearing rocks as crustal protoliths modified at depth along the contact with the ultramafic rocks of the Lherz body during their ascent towards shallower depths. These new data imply: (i) an Upper Triassic to Lower Jurassic origin for the main protolith of the sapphirine-bearing rocks, (ii) the metamorphism of this protolith along an active hot crust–mantle detachment during Cenomanian times with the involvement of metasomatic, brine-type fluids, and (iii) its brecciation during the exhumation of the material due to the evolution of the detachment, followed by subsequent sedimentary reworking of the metamorphic material.

I. Introduction

Sapphirine ($(Mg,Fe,Al)_8O_2(Al,Si)_6O_{18}$); Moore, 1969) is a relatively rare mineral which records either ultrahigh-temperature conditions in silica-rich systems (*e.g.* Harley & Motoyoshi, 2000, Wheller & Powell, 2014) or high temperature and intermediate pressure conditions in silica-

99 poor systems. In the absence of quartz, sapphirine is described as the product of
100 metamorphic evolution of three main types of protoliths, namely: mafic and ultramafic rocks
101 (*e.g.* Morishita *et al*., 2001; Jöns & Schenk, 2008; Feneyrol, 2012), crustal rocks (*e.g.* Arima &
102 Barnett, 1984), and evaporitic deposits or metasomatic assemblages implying fluids (*e.g.*
103 Schreyer & Abraham, 1976; Grew, 1988; Harley, 1993; Engvik & Austrheim, 2010). In the
104 Pyrenean belt, Monchoux (1969) first described sapphirine at the northern edge of the Étang
105 de Lherz lherzolite body, more commonly called the Lherz body (Ariège, France; Fig. 1), in a
106 context involving both ultramafic rocks and metasediments. There, sapphirine crystals occur
107 in layered clastic deposits characterized by uncommon mineral associations including Mg-
108 amphibole, aluminous orthopyroxene, spinel and kornerupine, which is a rare boron-bearing
109 sorosilicate ($Mg_3Al_6(Si,Al,B)_5O_{21}(OH)$; *e.g.* Grew *et al.*, 1990; Hawthorne *et al.*, 2009). This
110 clastic assemblage consists of polymictic breccias and sandstones exposed in a contact zone
111 between the lherzolites and Mesozoic metasediments, mainly marbles (Monchoux, 1969).
112 These marbles underwent the high-temperature, low-pressure (HT-LP) Mid-Cretaceous
113 Pyrenean metamorphic event which is recognized all along the North Pyrenean Zone (NPZ;
114 Ravier, 1959; Albarède & Michard-Vitrac, 1978; Montigny *et al.*, 1986; Golberg & Maluski,
115 1988; Dauteuil & Ricou, 1989; Golberg & Leyreloup, 1990; Clerc & Lagabrielle, 2014; Clerc *et*
116 *al.*, 2015; Ducoux, 2017). Golberg & Leyreloup (1990) were the first to ascribe this
117 metamorphic event to a crustal thinning episode in the future NPZ.
118 The Lherz sapphirine-bearing rocks were first interpreted as deriving from lower
119 continental crust lithologies modified at depth along the contact with the ultramafic rocks of
120 the Lherz body during their ascent towards shallower depths (Monchoux, 1970, 1972a). This
121 interpretation needs to be revisited because back then, the processes leading to mantle
122 exposure at the Earth's surface were poorly understood and models of subcontinental mantle

123 exhumation along detachment faults were not yet applied to the Pyrenean case (*e.g*.
124 Lagabrielle & Bodinier, 2008; Jammes *et al*., 2009; Duretz *et al.*, 2019). In addition, the North
125 Pyrenean Cretaceous metamorphic event was not recognized as the result of crustal thinning
126 but was thought to be related to the early compressional phases of the Pyrenean orogeny
127 (*e.g.* Choukroune, 1970; Debroas, 1978).

128 The occurrence of mantle outcrops in the distal part of passive continental margins is
129 now extensively documented (*e.g.* Boillot *et al.*, 1980; Espurt *et al*., 2009; Gillard *et al*., 2016;
130 Péron-Pinvidic & Osmundsen, 2016). These recent advances allow for fruitful comparisons
131 between passive margins and some units of the Pyrenean belt and thus provide key
132 arguments to unravel the significance of the geological associations found in the vicinity of
133 mantle exposures in the NPZ (*e.g.* Masini *et al.*, 2014; Tugend *et al.*, 2015; Corre *et al.*, 2016).
134 In this paper, we present the results of a detailed petrographic study of the formations
135 exposed at the northern border of the Lherz body, in two of the sites where Monchoux (1970,
136 1972a, b) described the sapphirine-bearing rocks. Our aim is to identify the protolith(s) and
137 the geological processes responsible for the formation of such uncommon mineral
138 associations and to explain their juxtaposition with exhumed mantle peridotites.

139

140 II. Geological setting

141 A. The North Pyrenean Zone and the Aulus Basin

142 The Pyrenean belt results from the collision between the Eurasian and Iberian plates
143 that started during the Santonian (*e.g*. Garrido-Megias, 1972; Olivet, 1996; García-Senz, 2002;
144 Rosenbaum *et al.*, 2002; McClay *et al*., 2004; Handy *et al.*, 2010). This double-verging orogen
145 is classically divided into three main structural domains: the North and South Pyrenean Zones,
146 composed of Mesozoic and Cenozoic sediments, and the Axial Zone exposing Paleozoic

147 basement rocks. The Axial Zone is separated from the NPZ by the North Pyrenean Fault (NPF)
148 (Fig. 1.1). The NPZ is characterized by a series of inverted basins that opened in the Albian-
149 Cenomanian times and that host about forty different fragments of subcontinental peridotites
150 (*e.g.* Lacroix, 1894; Bodinier *et al.*, 1987; Fabriès *et al.*, 1991; Henry *et al.*, 1998). These
151 mantle bodies crop out within Mesozoic metasediments that underwent a HT-LP
152 metamorphic evolution that took place between the Albian and Santonian times (110 - 85
153 Ma: Albarède & Michard-Vitrac, 1978; Montigny *et al.*, 1986; Golberg & Maluski, 1988; Clerc
154 *et al.*, 2015). The opening of the NPZ basins occurred in response to the counterclockwise
155 rotation of Iberia, which was accommodated by a sinistral transtensional motion along the
156 future NPF (Olivet, 1996; Sibuet *et al.*, 2007; Gong *et al.*, 2008). The NPZ also includes
157 different isolated Paleozoic North Pyrenean Massifs (NPM) that represent remnants of its
158 original continental basement. These massifs experienced three metamorphic episodes,
159 namely the Hercynian, Permian and Cretaceous events. The Hercynian orogeny (*ca.* 350-300
160 Ma) in the Pyrenees is characterized by a polyphased deformation, accompanied by a HT-LP
161 metamorphism, migmatization and granitic magmatism (*e.g.* Denèle *et al.*, 2014). During the
162 Permian, the opening of sedimentary basins in the Pyrenees (*e.g.* Bixel & Lucas, 1987; Lago *et*
163 *al*., 2004; Saspiturry *et al.*, 2019) induced reheating of the NPM (*e.g.* Bixel & Lucas, 1987;
164 Briqueu & Innocent, 1993; Lago *et al*., 2004; Denèle *et al*., 2012; Asti *et al*., 2019). Then, the
165 Cretaceous extensional event resulted in an early crustal thinning and in fragmentation of the
166 NPM (*e.g.* Costa & Maluski, 1988; Vauchez *et al.*, 2013). Evidence for major fluid circulations
167 linked to this last thinning episode was found in some NPM, including talc-enriched faults
168 (Schärer *et al.*, 1999; Boutin *et al*., 2016) and hydrothermal albitites (Boulvais *et al.*, 2007;
169 Poujol *et al.*, 2010; Fallourd *et al*., 2014). The Albian-Santonian HT metamorphic event was
170 assigned to the latter crustal thinning episode (Golberg & Leyreloup, 1990) and was further

correlated to the exhumation of the subcontinental mantle rocks (Lagabrielle & Bodinier, 2008; Clerc & Lagabrielle, 2014). The peak-temperature estimates obtained for the extensional Cretaceous event in the NPZ using Raman spectroscopy of the carbonaceous matter (RSCM) were measured in the Mesozoic metasediments of the Aulus Basin (Fig. 1.2.). Values are grouped around 550°C, reaching 625°C in one sample (Clerc *et al.*, 2015).

During the past decade, the North Pyrenean subcontinental peridotite bodies have been repeatedly studied in order to unravel the processes of mantle exhumation in the Cretaceous Pyrenean basins (*e.g.* Lagabrielle & Bodinier, 2008; Jammes *et al.*, 2009; Clerc *et al.*, 2012; Clerc & Lagabrielle, 2014; De Saint Blanquat *et al.*, 2016; Lagabrielle *et al.*, 2016; DeFelipe *et al.*, 2017; Lagabrielle *et al.*, 2019). Several recent studies argue for a tectono-sedimentary model for the emplacement of the ultramafic rocks and associated breccias (Lagabrielle & Bodinier, 2008; Lagabrielle *et al.*, 2010, 2016; Clerc *et al.*, 2012; Clerc & Lagabrielle, 2014). In these models, the subcontinental Pyrenean mantle was exhumed along detachment faults and exposed locally on the floor of the narrow NPZ basins during the Cretaceous rifting event, under high thermal conditions.

Recent reconstructions based on geological investigations along the NPZ basins led to define a peculiar architecture for the Pyrenean paleo-passive margin controlled by a high thermal regime, thus contrasting with classical models of passive margins exemplified by the Iberia-Newfoundland case (Péron-Pinvidic & Manatschal, 2009). This led Clerc & Lagabrielle (2014) and Clerc *et al.* (2016) to propose a mechanism of rifting in the distal margin domain involving the boudinage of the continental crust under a mobile Mesozoic pre-rift cover detached from the basement along Late Triassic clays and evaporites decoupling layers. A

193 more brittle behaviour characterizes the proximal margin domain. This model was
194 corroborated by recent numerical modelling work (Duretz *et al.*, 2019).
195
196 B. Geological content and interpretations of the Lherz breccias
197 The Aulus Basin exposes Mesozoic metasediments and two major ultramafic
198 exposures: the Lherz and Freychinède bodies. Small gabbro and meta-ophite (Late Triassic
199 mafic hypovolcanic rocks) bodies are also found in the vicinity of the ultramafics (Fig. 1.2).
200 Metasediments exposed close to both Lherz and Freychinède bodies are massive carbonates
201 and breccias often referred to as the Lherz breccias (*e.g.* Lacroix, 1894; Choukroune, 1973,
202 1976; Ternet *et al.*, 1997). Previous studies investigated in detail the petrography of the Lherz
203 breccias and discussed their possible modes of emplacement either as ~~(~~sedimentary breccias
204 (Lacroix, 1892; Choukroune, 1973), tectonic breccias (Lacroix, 1900; Ternet *et al.*, 1997;
205 Debroas *et al*., 2010, explosion breccias (Avé Lallemant, 1968; Minnigh *et al.*, 1980), or
206 tectono-sedimentary breccias (Lagabrielle *et al.*, 2016 and references therein). These studies
207 first pointed to the great variability in the breccia types which range from monomictic
208 carbonate breccias to pure ultramafic breccias. Between these two end-members, polymictic
209 breccias are composed of various proportions of ultramafic and Triassic to Early Cretaceous
210 carbonate clasts (Clerc *et al.*, 2012). The Lherz breccias also contain clasts of meta-ophite,
211 enstatite-gabbro, and minor amounts of Paleozoic crustal rocks.
212 A progressive transition from the peridotite rocks to the surrounding breccias is
213 observed around the Lherz and Freychinède bodies. At an increasing distance from the
214 borders of the ultramafic bodies, one gradually observes: (i) ultramafic breccias with a calcite-
215 rich matrix (ophicalcites; Lagabrielle & Bodinier, 2008; Clerc *et al.*, 2014), (ii) monomictic

ultramafic breccias with an ultramafic-rich matrix, (iii) polymictic ultramafic and marble breccias and (iv) monomictic marble breccias (Lacroix, 1894; Monchoux, 1970).

The age of deposition of the breccias is a matter of debate because of the lack of stratigraphic or paleontological constraints. The observation of cracks in the peridotite infilled by breccias indicates that deposition of breccias postdates or is synchronous with exhumation of the peridotite to the basin floor (Lagabrielle & Bodinier, 2008). Lherz breccias clasts are dominantly carbonates that underwent metamorphism leading to scapolite and amphibole-bearing foliated marbles. This implies a post-metamorphic or syn-metamorphic origin for the breccias deposition.

An anchizonal to epizonal thermal event leading to neoformation of muscovite and paragonite has been characterized in the carbonatic pelitic metasediments of the Turonian-Senonian flysch of the Aulus Basin (80 Ma; Montigny *et al.* 1986). This is confirmed by peak metamorphic temperatures reaching 350°C recently obtained in a tectonic slice of this flysch pinched along the southern rim of the Aulus Basin (Clerc *et al.*, 2015). Dating results obtained in the NPZ show that the thermal anomaly affecting the north Pyrenean basins may have lasted from 107 Ma to 80 Ma, *i.e*. during almost 27 My (see complete references in Clerc *et al.*, 2015). This time span is large enough for a succession of events to develop in the sedimentary cover of the Aulus Basin, including: (i) high-temperature metamorphism during the ascent of the peridotites towards shallow levels, (ii) exhumation and disaggregation to the seafloor, followed by sedimentation of the Lherz breccias, (iii) diagenesis and renewed thermal metamorphism following burial under Late Cretaceous flysch sequences.

Lagabrielle *et al.* (2016) used the geological constraints summarized above to construct a tectono-sedimentary model for the emplacement of the NPZ peridotites and associated metasediments. This model contrasts with former interpretations of the Lherz

body as tectonic slices or olistolith (*e.g.* Vielzeuf & Kornprobst, 1984; Lagabrielle *et al.*, 2010). In their 2016's model, Lagabrielle *et al.* propose that the Lherz peridotite is exhumed along a detachment fault and thus represents the bottom of the Aulus Basin. The Mesozoic sedimentary formations, decoupled from the Palaeozoic basement, are juxtaposed on top of the Lherz body and thereby suffer metamorphism and deformation. Their brecciation and re-sedimentation occurs during their exhumation. This model considers most of the lithologies exposed in the Aulus Basin but it needs refinement since it does not account for the presence of the sapphirine-bearing rocks along the contact with the ultramafic rocks. Following Clerc *et al.* (2012) and further studies, the geological setting of the sapphirine-bearing rocks implies to consider this formation as the lowermost levels of the Lherz tectono-sedimentary breccias. Therefore, the sapphirine-bearing rocks are good candidates to represent the first formation emplaced over the detachment fault that allowed the peridotite of the Lherz body to be exhumed towards upper crustal levels and finally exposed on the floor of the former Aulus Basin.

III. Geological description of sampling sites and analytical methods

The sixteen samples of sapphirine-bearing sandstones and breccias studied here were collected at two sites which were first described by P. Monchoux (exposures 1 and 3 in: Monchoux, 1970, 1972a, b), hereafter referred to as sites 1 and 2 (Fig. 1.2 and 2.1). The other exposures described by P. Monchoux, all located along the contact between the Lherz body and the Mesozoic marbles and breccias of the NPZ, have disappeared under the vegetation.

At site 1 (42°48'30.52"N 1°22'52.85"E), the sapphirine-bearing sandstones are present along an ancient road-cut, in front of the Etang de Lherz restaurant. The exposure has been cleared on a length of 8 m. The sandstones and breccias form a layered sequence with a

264 rough vertical bedding defined by alternating dark-brown, orange and light-grey layers (Fig.
265 2.1). The thickness of layers varies from some centimetres to one metre and variations in
266 colours are clearly linked to variable lithological compositions. At first sight, the exposure
267 displays four types of clastic layers, namely the A, B, C and D layers (sometimes recurrent)
268 separated by rather sharp contacts (Fig. 2.1, 2.2). (i) Layer A is the dominant type. It
269 corresponds to light grey, coarse sandstones composed of white and grey grains with planar
270 to acicular outlines. Some of the grains show shinning cleavages, evoking micas and
271 amphiboles. Based on HCl tests, some portions of Layer A contain calcite, others do not. (ii)
272 Layer B corresponds to dark-brown layers of ultramafic breccias and microbreccias composed
273 of dominant angular clasts of serpentinized lherzolite in a sandy matrix with an ultramafic
274 composition. The largest clasts are up to 10 cm long (Fig. 2.2). (iii) Layer C is represented by
275 breccias and sandstones made of dominant ultramafic and minor cm-sized clasts of a
276 granoblastic mafic rock (Fig. 2.3). The latter clasts, which exhibit mm-sized white and black
277 crystals, typically derive from the metamorphism of Triassic ophite (Azambre *et al.*, 1987). (iv)
278 Layer D is a coarse breccia made of a mix of the lithologies forming the previous A, B and C
279 layer types. It is composed of cm- to dm-sized angular clasts of ultramafic rock, white
280 sandstones and microbreccias, and Late Triassic meta-ophites (Fig. 2.4). It also includes clasts
281 of a black rock spotted by white material corresponding to the so-called “micaceous hornfels”
282 (“cornéennes micacées”, Lacroix, 1894) largely exposed some kilometres south of the studied
283 exposures, at Col d’Agnès (Ternet *et al.*, 1997). The “micaceous hornfels” have an unequivocal
284 aspect and are composed of an association of scapolite and phlogopite which derive from the
285 metamorphism of Upper Triassic to Lower Jurassic evaporitic clays during the Cretaceous HT
286 Pyrenean event (93 ± 3 Ma; Ravier & Thiébaut, 1982; Montigny *et al.*, 1986).

At site 2 (42°48'26.78"N 1°23'7.97"E), located along the north-eastern border of the Lherz body (Fig. 1.2), a portion of the former exposure 3 described by Monchoux (1972a, b) was partly cleared on both sides of a gully, over a few metres between outcrops of the massive peridotite and outcrops of pure marble breccias (Fig. 3.1). The outcrop consists of a pale-green to light-grey microbreccia showing a rough bedding dipping to the south-east. Sandstones layers are interbedded and crossed-stratification can be locally observed (Fig. 3.2, 3.3). The microbreccia contains numerous dm-sized angular clasts of variable lithologies including “micaceous hornfels” and poorly serpentinized lherzolites (Fig. 3.4). The ultramafic clasts are more abundant close to the contact with the Lherz body. The entire outcrop is calcite-rich.

Although we could not observe the exact exposures described and sampled by Monchoux (1970, 1972a, b), our field observations, even before any microscopic analysis, clearly match his description, in particular (i) the high diversity of the clastic layers components with frequent mixing of light-coloured material and ultramafic material, and (ii) at site 2 a progressive transition from the sapphirine-bearing rocks to the pure marble breccias and microbreccias that dominantly form the overlying Lherz breccia. This transition is depicted by the white dotted line 1 in Figure 3.1.

Our sixteen samples allow to recover the diversity of types described by Monchoux (1970, 1972a, b). Eleven samples were collected at site 1 (BCOR 71, BCOR 72, BCOR 73, LHZ 49, LHZ 7a, Momo 1, Momo 2, Momo 2a, Momo 2b, Momo 5 and Momo 6). Five samples were collected at site 2 (BCOR 67b, BCOR 68a, BCOR 68b, LHZ 114a and NR 94). Given the thorough mineralogical studies carried out on the same material by Monchoux (1970, 1972a, b) and by Abraham *et al.* (1977), we rather focus on textures, complementary mineral

compositions and mineral inclusion patterns that could give clues as to the nature and origin of this uncommon material.

Thin sections were prepared for each sample for microscopic observation and electron microprobe (EMP) analyses. The latter were performed in the French Research Institute for Exploitation of the Sea (Ifremer) in Plouzané (Brest, France) using a CAMECA SX100 instrument, equipped with five spectrometers and a full set of analysing crystals. Further imaging and analyses in energy-dispersive mode (EDS) were carried out on five samples using a Zeiss Σigma™ field-emission-gun scanning electron microscope equipped with a large-area (50 mm^2) EDS silicon drift detector, X-Max Oxford Instruments, at ENS Paris. Raman analyses for phase characterization in sample BCOR 72 were obtained using the Renishaw inVia spectrometer at ENS Paris, with a 514.5 nm argon laser focused through a DMLM Leica microscope. The signal was filtered by edge filters, dispersed by a 1200 or 1800 grooves/mm grating and analysed with a Peltier cooled RENCAM CCD detector, using Si as calibration standard.

In addition, laser ablation inductively coupled mass spectrometry (LA-ICP-MS) U-Pb dating was performed on some rutile grains using an ESI NWR193UC Excimer Laser coupled to an Agilent quadripole 7700x ICP-MS available at Géosciences Rennes. Information regarding the analytical procedures can be found in the *Supplementary Material SM1*.

IV. Results

A precise description of each studied sample is provided in the *Supplementary Material SM2*.

A. General petrography

Three main types of samples can be distinguished on the basis of their mineralogical compositions (Tab. 1, see also Tab. 2):

334 - Type I was collected in coarse breccias of layer D at site 1 and corresponds to portions of
335 polymineralic clasts (Fig. 2);
336 - Type II was collected in layer A at site 1 and at site 2. It corresponds to microbreccias with a
337 calcitic cement and made of either 100% of monomineralic clasts or scarce polymineralic
338 clasts associated with predominant monomineralic clasts;
339 - Type III was collected in layers A, B and C at site 1 and corresponds to microbreccias devoid
340 of any calcitic cement and made of either 100% of monomineralic clasts or of scarce
341 polymineralic clasts associated with predominant monomineralic clasts.
342 Type I samples are very homogeneous (Tab. 2, Fig. 4). Samples BCOR 71, Momo 2 and
343 Momo 6 are made of scapolite (with anorthite, phlogopite, tourmaline and apatite inclusions),
344 phlogopite, diopside, tourmaline and scarce epidote and zoisite. They correspond to clasts of
345 the emblematic Pyrenean "micaceous hornfelses" (Lacroix, 1894), *i.e.* metamorphic Upper
346 Triassic to Lower Jurassic sediments and evaporites. Sample Momo 5 is made of scapolite,
347 diopside, anorthite, phlogopite, potassian hastingsite, tourmaline and calcite and thus
348 corresponds to some intermediate facies between the "micaceous hornfelses" and the
349 surrounding marbles (Ravier & Thiébault, 1982).
350 Type II samples are also rather homogeneous (Fig. 5). Six of the eight samples include
351 sapphirine crystals, and the other two samples include minerals that commonly occur
352 together with sapphirine in our samples (Tab. 2). The complete suite in Type II samples is:
353 sapphirine (with Cl-rich apatite and rutile inclusions), enstatite (with anhydrite, F- and Cl-rich
354 apatite, clinochlore and zircon inclusions), aluminous spinel, Mg-amphiboles (anthophyllite–
355 gedrite solid solution with rutile inclusions), Ca-amphiboles (pargasite with F- and Cl-rich
356 apatite, clinochlore and zircon inclusions; tschermakite), tourmaline, rutile, vermiculite and
357 smectite. The scarce polymineralic clasts are made of sapphirine and Mg-amphibole of the

gedrite–anthophyllite series, of sapphirine and aluminous spinel, of anthophyllite and vermiculite, of sapphirine and vermiculite, or of sapphirine, vermiculite and anthophyllite (Tab. 2). A striking feature in these samples is the abundance of kinked vermiculite with open cleavages and ponytail edges (*e.g.* Fig. 5.3). These features suggest that vermiculite derives from the transformation of a former phyllite, likely phlogopite or aspidolite. Monomineralic and polymineralic clasts are all angular, except vermiculite.

Type III samples are far more heterogeneous in composition (Tab. 2).

- sample BCOR 72 is composed of an accumulation of millimetric to plurimillimetric isolated crystals, dominantly vermiculite and amphiboles with, in order of decreasing abundance: gedrite, pargasite, vermiculite, aluminous enstatite, kornerupine, sapphirine, diopside, tourmaline, rutile and white mica (Tab. 2). Very scarce polymineralic clasts are observed (Fig. 6.1). One millimetric kornerupine crystal shows a subhedral shape (Fig. 6.2). A very fine-grained matrix composed of the previously listed minerals and devoid of any calcite can be observed locally.

- sample Momo 1 also appears as a friable orange-brown sandstone. It includes angular monomineralic clasts and subangular to rounded polymineralic clasts (Fig. 6.3 and 6.4). Isolated detrital minerals include: magnesio-hornblende, enstatite, chromian hercynite, phlogopite, muscovite, clinopyroxene, quartz, chlorite and several types of plagioclase (An18–58). Polymineralic clasts include: unserpentinized (Fig. 6.4) and serpentinized ultramafic rocks, meta-ophite (Fig. 6.4, Tab. 2), as well as one clast of granitic gneiss. A single clast composed of olivine, plagioclase (An56.9–58.1) and enstatite was also observed. This clast is reminiscent of rocks that are known in the Aulus Basin, namely a Cretaceous alkaline enstatite-gabbro (Les Plagnaux gabbro) (Montigny *et al.*, 1986; Ternet *et al.*, 1997) or the cumulate portion of a Triassic ophitic intrusion (Azambre *et al.*, 1987).

382 - sample LHZ 49 is an orange-brown fine-grained sandstone exclusively made up of angular,
383 submillimetric monomineralic clasts (Fig. 6.5) from a dominant ultramafic protolith. Clasts
384 include: olivine (Fo89.9–91.0), diopside, enstatite, titanian pargasite, hercynite, chromian
385 hercynite, chlorite and minor quartz (Tab. 2).
386 - sample BCOR 73 is a yellowish phyllite-rich sandstone which contains a single centimetric
387 subrounded greenish polymineralic clast (Fig. 6.6). The sandstone is composed of angular
388 monomineralic grains of various nature (in decreasing order of abundance): vermiculite,
389 pargasite, clinopyroxene, scapolite, a green spinel, rutile and tourmaline (Tab. 2). The
390 centimetric greenish subrounded clast derives from a scapolitized amphibolite with
391 clinopyroxene and some vermiculite. This mineral assemblage derives from a micaceous
392 hornfels (Lacroix, 1894; Ravier & Thiébault, 1982), in which primary phlogopite or aspidolite
393 was transformed into vermiculite. This clast is surrounded by vermiculite, oriented roughly
394 parallel to the clast border (Fig. 6.6).
395 B. Textural analysis
396 The numerous mineral species that compose the studied samples are all represented
397 by angular and broken monomineralic clasts that obviously derive from a collection of various
398 rock-types (Fig. 4 to 6, Tab. 2). In most cases these clasts are submillimetric fragments of
399 crystals that are disconnected from their original protolith. We also observe larger isolated
400 crystals, millimetric to plurimillimetric in size (centimetric in rare instances, as in samples
401 BCOR 68a and NR 94), of the same species as the submillimetric clasts of the matrix. The
402 largest clasts may be surrounded by submillimetric debris of the same mineral species (Fig. 7).
403 Most of the polymineralic clasts are millimetric to plurimillimetric in size. They are fractured
404 with irregular borders (except in sample Momo 1). In most samples of types II and III which

include both monomineralic and polymineralic clasts, the mineral species of the monomineralic clasts are the same as those forming the polymineralic clasts.

In seven samples of types II and III, a layering is observable macroscopically (samples Momo 1, Momo 2b and NR 94) or microscopically (samples LHZ 49 and LHZ 7a, BCOR 72 and BCOR 73 (Fig. 8, see also Fig. 6.5). The layers are usually characterized by the accumulation of one or two specific minerals. Representative examples are samples BCOR 72 (Fig. 9) and BCOR 73 which both display overabundances of amphiboles and vermiculite. In these cases, the layering is also outlined by the alignment of the planar minerals (in particular vermiculites). In some examples, layering is locally interrupted against polymineralic clasts, the borders of which are coated by planar minerals (*e.g.* sample BCOR 73, Fig. 6.6). In sample Momo 1, layering results from the accumulation of polymineralic clasts of different compositions (Fig. 8.2). In addition, each layer may exhibit a grain-size sorting, as also observed in sample NR 94.

C. Definition of the sapphirine-bearing mineral suite (SBMS)

The petrographic study of the sixteen thin sections of sapphirine-bearing rocks reveals that some polymineralic clasts or isolated minerals derive from well-known protoliths such as ultramafic rocks, meta-ophites, micaceous hornfels and, rarely, Paleozoic basement rocks. This is the case for our Type I and part of our Type III, as reported above. Nevertheless, a large portion of the sapphirine-bearing clastic suite is composed of mono- and polymineralic debris that derive from unknown protolith(s). This is the case for Type II and part of Type III samples. The complete mineral suite in these samples is: sapphirine + enstatite + aluminous spinel + Mg-amphiboles + Ca-amphiboles + kornerupine + accessory minerals (apatite, diopside, rutile, serpentine, smectite, tourmaline, vermiculite and a white mica) (Tab. 2). The high recurrence of these minerals found in association with sapphirine in our sample collection leads us to define a "sapphirine-bearing mineral suite", referred to as SBMS.

As reported above, most of the clasts observed in the sapphirine-bearing sandstones are monomineralic and isolated. However, rare clasts of polymineralic aggregates exhibiting textural equilibrium are observed in some samples. They are made of sapphirine and Mg-amphibole, of sapphirine and aluminous spinel, of anthophyllite and vermiculite, of sapphirine and vermiculite, or of sapphirine, vermiculite and anthophyllite (Tab. 2). The most frequent associations involve sapphirine and Mg-amphibole of the gedrite–anthophyllite series. These minerals are commonly intergrown, which suggests that they crystallized simultaneously (Fig. 5.1, 5.5, 5.6 and 6.1).

Finally, we point out that the assemblages represented by the SBMS derive from metamorphic source-rocks that have never been described so far in the Lherz area. In the following, our aim is to characterize these metamorphic source-rocks.

D. Mineral chemistry of the SBMS

Representative analyses of the main phases forming the SBMS are given in Tab. 3. The chemistry of some minerals of the SBMS uncommonly observed in the region is detailed in the following.

- **Sapphirine** occurs in seven samples (Tab. 2, Fig. 5.1, 5.3, 5.5, 5.6, see also Fig. 6.1 and Fig. 10.1). In the microbreccias, it appears as up to millimetre-size (LHZ 7a), pale blue to deep blue subhedral crystals, always fractured and commonly corroded. The corrosion gulfs are filled by calcite in Type II samples (Fig. 5.3, see also 10.1). Microprobe analyses show that the sapphirine-bearing clasts display high Mg content (X_{Mg} = Mg/(Mg+Fe_{total}) = 0.91-0.92), except in LHZ 7a for which X_{Mg} values of 0.83–0.86 may reflect a higher proportion of ferric iron, as suggested by the analysis of spinel. With 1.58(4) Si per formula unit (pfu), sapphirine is close to the classical 7:9:3 (Mg,Fe)O:Al_2O_3:SiO_2 composition (*e.g.* Podlesskii, 2010). It is nearly devoid of Cr_2O_3 (<0.06 wt%) and NiO (<0.02 wt%).

453 - **Kornerupine** occurs in sample BCOR 72 as a millimetric prismatic subhedral crystal and as
454 fragments with no relationship to each other (Fig. 6.2, see also 10.2). It contains 2.3 wt% B_2O_3
455 according to a wet chemical analysis (Monchoux, 1972a), 3.0 wt% according to EMP analysis
456 in Table 3. It is also characterized by a high X_{Mg} value (0.93) and low Cr_2O_3 (<0.04 wt%) and
457 NiO (<0.08 wt%) contents.
458 - **Aluminous enstatite** occurs as pale blue crystals in three samples (samples LHZ 114a, NR 94,
459 BCOR 72; Tab. 2). It shows a consistent X_{Mg} value of 0.90(1), Al_2O_3 contents from 1.89 to 3.48
460 wt%, with an average of 2.5 wt%, *i.e.* 5 mol% Mg-Tschermak (= $MgAl_2SiO_6$) component. This is
461 among the lowest Al contents in enstatite reported from sapphirine-bearing rocks. The TiO_2 (<
462 0.11 wt%), Na_2O (< 0.19 wt%) and Cr_2O_3 (< 0.5 wt%, mostly <0.3 wt%) contents are not
463 distinctive from enstatite from the Lherz lherzolite (Le Roux *et al.*, 2007, her corrected Table
464 2), but the low CaO contents are distinctive (< 0.21 wt%, *versus* 0.3 to 1.3 wt% in lherzolite).
465 - **Aluminous spinel** occurs as blue fragments in mono- or polymineralic clasts (Tab. 2, Fig. 5.4);
466 unlike the clasts of brown or green spinel, it cannot be traced back to common rock-types of
467 the area, either basement or ultramafic bodies. The low Cr_2O_3 (<0.1 wt%) and Fe_2O_3 contents
468 (< 0.05 Fe^{3+} pfu) as well as high Al and high X_{Mg} (> 0.8) are distinctive.
469 The above four mineral species are highly magnesian, as are most of the other species
470 of the SBMS. Indeed, gedrite, anthophyllite, pargasite, vermiculite and tourmaline all have
471 MgO ± Al_2O_3 ± SiO_2 (± B_2O_3) as their main constituents (Tab. 3).
472 Sapphirine crystals in samples BCOR 67b, BCOR 68a and BCOR 68b display apatite
473 inclusions (Tab. 2, Fig. 10.1) that are extremely rich in Cl (4.4-4.7 wt%, Tab. 4), close to
474 chlorapatite end-member. Kornerupine crystals bear Cl-rich apatite and anhydrite inclusions
475 (sample BCOR 72; Fig. 10.2). Aluminous enstatite bears inclusions of Cl-rich fluorapatite (1.93
476 wt% Cl and 2.02 wt% F on average) and of Sr-bearing anhydrite (0.42 wt% SrO on average)

477 which may also be associated (Fig. 10.3), and of clinochlore (sample NR 94; Tab. 2 and 4; Fig.
478 10.4). Ca-amphibole crystals also display rare apatite inclusions (sample NR 94).

479 ### E. U-Pb dating of rutile in samples BCOR 68a and b

480 Since the Pyrenees experienced three metamorphic episodes (see section II.A. above),
481 we performed a geochronological study on the only mineral found to be suitable for
482 geochronological dating: rutile (Tab. 2). U-Pb geochronology of rutile was conducted in-
483 context in samples BCOR 68a and b in order to constrain the age of the SBMS. Given their
484 very similar content and sampling location, we consider that these two samples derive from a
485 same (and still unknown) protolith and experienced the same geological processes (Tab. 2).

486 Twenty-six analyses were acquired on ten rutile grains (100 to 200 µm in length)
487 during two analytical sessions (Tab. 5). All analyses were acquired on monomineralic rutile
488 clasts, except three analyses which were performed on a similar rutile inclusion located within
489 a sapphirine crystal clast (S-301018a-1, S-301018a-2, S-301018a-3; BSE images are provided
490 in *Supplementary Material SM3*). Whatever their location, analyses show variable U (58-164
491 ppm) and Pb (1-441 ppm) contents with variable amounts of common Pb (f206% between 0
492 and 2.3%) (Tab. 5). In a Tera-Wasserburg diagram (Fig. 11), they all plot in a concordant to
493 discordant position (depending on the amount of common Pb) and define a well-constrained
494 lower intercept date of 98.6 ± 1.2 Ma (MSWD=1.6). This date is equivalent within error to the
495 ^{207}Pb-corrected date (calculated using Stacey and Kramers (1975) terrestrial Pb evolution
496 model calculated at 100 Ma) of 98.9 ± 0.7 Ma (MSWD=1.4, N=26).

497

498 V. Discussion: origin of the sapphirine-bearing rocks

499 A. Evidence for a tectono-sedimentary origin

The petrological descriptions of the sixteen samples collected at sites 1 and 2 shows that the sapphirine-bearing sandstones and breccia formation is an assemblage of beds of various mineralogical composition and grain size with thicknesses varying from some millimetres to some decimetres.

In section IV.B., we describe microbreccia and sandstone samples made of the accumulation of highly fragmented minerals and polymineralic clasts. We show that in most samples, monomineralic clasts exhibit angular shapes, sometimes with little displacement between fragments, and are of the same species as minerals forming the polymineralic clasts. This reinforces the hypothesis of an in-situ disaggregation of the largest clasts to form the submillimetric monomineralic clasts. However, in two samples some monomineralic submillimetric clasts do not have their polymineralic counterpart (*e.g.* quartz in sample Momo 1; pargasite, rutile and green spinel in sample BCOR 73), which implies clast mixing at a scale larger than the hand specimen size. Our textural analysis also reveals a layering often defined by the accumulation of one or two specific minerals or polymineralic clasts in seven samples, as well as grain-size sorting at microscopic and macroscopic scales. Those samples which concentrate only few mineralogical species do not correspond to any classical protolith of metamorphic or plutonic origin and can be regarded as placer deposits.

These observations collectively imply that the sapphirine-bearing sandstones and breccias accumulated through sedimentary processes in a context of active tectonics allowing for the brecciation of a variety of lithological assemblages. Identifying all the involved lithologies, especially the protolith(s) of the SBMS is thus necessary before any attempt at understanding the geodynamic setting in which those brecciation and mixing processes occurred.

B. Deciphering the sources of the material reworked in the sapphirine-bearing rocks

1- Unequivocal sources

Several sources can be unambiguously identified through the mineralogical composition of the studied microbreccia clasts, especially the polymineralic ones. These sources include:

(i) Mantle rocks, either fresh or serpentinized, as shown by polymineralic clasts including forsterite, serpentine, enstatite, diopside, hercynite or chromian hercynite and by serpentine, hercynite or chromian hercynite isolated crystals;

(ii) Upper Triassic to Lower Jurassic meta-ophites (Azambre *et al.*, 1987) as shown by polymineralic clasts including magnesio-hornblende, diopside and plagioclase hosting abundant solid and fluid inclusions, and by isolated plagioclase crystals with the same inclusions;

(iii) Upper Triassic to Lower Jurassic-deriving “Micaceous hornfelses” (Lacroix, 1894; Ravier & Thiébault, 1982) are identified through polymineralic clasts including scapolite, anorthite, diopside, phlogopite, tourmaline, epidote or apatite and through isolated tourmaline crystals.

(iv) Continental basement rocks, represented by one single polymineralic clast made of quartz, phlogopite and muscovite.

The conclusion from this first inventory is that, apart from lherzolites and very scarce basement rocks, the unequivocally identified protoliths that fed the sandstones and breccias derive from an Upper Triassic to Lower Jurassic sequence, which is composed of evaporitic sediments hosting ophites and is affected by the HT-LP Cretaceous metamorphic episode. No protolith containing the complete mineralogy of the SBMS exist in the vicinity of our study zone. The source(s) of the SBMS still have to be identified.

3- Source(s) of the SBMS

a) Sapphirine-bearing rocks in the Pyrenees: a comparison

548 The present location of the SBMS is the interface between the Lherz exhumed mantle
549 and the Mesozoic marbles and breccias. A comparable situation is encountered for very
550 similar rocks located 40 km East of Lherz, in the Bois de Fajou site (Monchoux, 1970; Fig. 1.1).
551 The latter author also mentioned panning concentrates containing euhedral sapphirine
552 crystals from catchments in the Central Pyrenees, not far from lherzolite bodies (Fig. 2 in
553 Monchoux, 1972a). This strengthens the idea of considering the sapphirine-bearing rocks as
554 the lowermost levels of the Lherz breccia.
555 In the Pyrenees, sapphirine is also a component of mineral assemblages commonly
556 involved in major contact zones between mantle and crust, formed under granulitic
557 conditions. In that respect, sapphirine-bearing assemblages have been reported from both
558 the Castillon North Pyrenean Massif and in Caussou, only 30 km away from the Lherz body
559 (NPZ, Ariège, France; Fig. 1.1). In the Castillon Massif, sapphirine was described in
560 amphibolites and in corundum-bearing anorthosites that crop out in contact zones between
561 mantle-derived peridotites and crustal kinzigites (Roux, 1977). These sapphirine-bearing
562 amphibolites were interpreted as crustal rocks metamorphosed at the contact with lherzolites
563 (Vielzeuf & Kornprobst, 1984). In Caussou, rare sapphirine has been reported from
564 amphibole-rich peridotites (Conquéré, 1978).
565 The previously referenced settings do not yield proper images of the SBMS because: (i)
566 sapphirine crystals are anhedral in these examples; (ii) no boron-bearing mineral (tourmaline,
567 kornerupine) nor mineral inclusion (Cl- and F- rich apatite, tourmaline, anhydrite) suggesting
568 the involvement of evaporites or evaporitic brines have been observed so far in those
569 assemblages; (iii) the assemblages commonly display coronitic textures, which are not
570 recovered even as relics in the SBMS and (iv) they display different mineral assemblages,
571 notably with mineral components (K-feldspar, quartz...) deriving from the surrounding crustal

572 rocks. Moreover, sapphirine is nearly devoid of Cr_2O_3 (<0.06 wt%) and NiO (<0.02 wt%) in our
573 sample collection, thus showing no direct evidence for mantle contribution. Therefore, none
574 of the assemblages from the Castillon Massif and from the Caussou mantle body is a suitable
575 candidate as source of the SBMS in the Lherz clastic deposits. Even a mix of several selected
576 debris from these different sources will never reconstitute the SBMS. The lack of garnet in the
577 Lherz SBMS is particularly significant in this respect, as well as the lack of quartz and –
578 feldspars debris that would have necessarily been a major contribution to our clastic
579 association since, in the Castillon massif, the rare sapphirine-bearing rocks are hosted by
580 dominant kinzigites. In summary, up to the present day, a suitable protolith for the SBMS is
581 unknown in the entire Pyrenees.

582 b) Sapphirine-bearing rocks worldwide: the evaporitic signal

583 Most sapphirine occurrences worldwide are linked to mafic and ultramafic rocks at
584 granulite-facies conditions (*e.g.* Morishita *et al.*, 2001; Jöns & Schenk, 2008; Chetouani *et al.*,
585 2016). However, in several localities, a different type of sapphirine-bearing rocks is described
586 and attributed to metamorphism of either evaporite deposits or of metasomatic assemblages
587 implying fluids of meteoric, evaporitic or hydrothermal origin. An emblematic example is the
588 pelitic whiteschists that occur as layers in talc-bearing series in Sar-e Sang (Afghanistan).
589 There, sapphirine is found together with chlorite, cordierite, corundum, gedrite, kyanite,
590 phlogopite, Na-plagioclase, minor pyrite, quartz, rutile, sillimanite, talc, tourmaline, and
591 xenotime (Schreyer & Abraham, 1976), or with enstatite, forsterite, kornerupine, magnesite,
592 phlogopite and spinel (Grew, 1988). In both cases, the authors interpret these rocks as highly
593 metamorphosed pelitic sediments associated with evaporite deposits. In Ødegarden Verk
594 (southern Norway), sapphirine is described in association with scapolite, Ca-amphibole,
595 clinopyroxene, phlogopite, enstatite, rutile, chlorapatite and talc in scapolitized metagabbros

596 in relation with metasomatism implying brine circulation (Engvik & Austrheim, 2010). In
597 Vestfold Hills (East Antarctica), sapphirine associated with enstatite and spinel is reported in
598 metasomatized, highly magnesian granulites hosted by paragneisses derived from evaporitic
599 mudstones (Harley, 1993).

600 c) Potential protolith(s) of the SBMS: cataclastic and metasomatized Keuper rocks?

601 As demonstrated by the microprobe analyses of Table 3, the protolith(s) of the SBMS
602 must be extremely rich in Al_2O_3 and MgO. This is consistent with former bulk-rock analyses by
603 Monchoux (1972a, Tab. 6), even though the analysed rocks are not direct witnesses of their
604 protolith(s) due to their tectono-sedimentary nature. The presence of mineral species such
605 as÷ (i) boron-bearing kornerupine, (ii) F-, Cl- and Sr-rich apatite, and (iii) anhydrite inclusions in
606 several minerals, points to the involvement of evaporites in producing the peculiar protolith
607 of the Lherz SBMS. It is worth noting that Upper Triassic metasediments are present close to
608 the southern border of the Lherz body, at Col d'Agnès (Ravier & Thiébault, 1982; Ternet *et al.*,
609 1997). These sediments underwent the HT-LP Cretaceous metamorphism and reached
610 temperatures in the range of 550-600°C coeval with mantle exhumation in the Aulus Basin
611 (Clerc *et al.*, 2015).

612 Cataclastic and metasomatized Keuper rocks are commonly found in shear zones
613 related to the major tectonic discontinuities in the NPZ, notably the North Pyrenean Frontal
614 Thrust (NPFT; *e.g.* Betchat and Bonrepaux, Central Pyrenees; Gleizes, 1971; Thiébaut *et al.*,
615 1988, 1992) and the NPF (*e.g.* Larrau-Sainte-Engrâce; Thiébaut *et al.*, 1992). At Betchat and
616 Bonrepaux, a brecciated Late Triassic formation metamorphosed under lower epizonal
617 conditions forms the sole of the NPFT (Gleizes, 1971; Thiébaut *et al.*, 1988, 1992). It is made
618 of gypsum lenses that host dominant magnesian (chlorite, dolomite, pargasite, phlogopite,
619 talc) and aluminous (chlorite, scapolite, phlogopite) minerals, with minor celestite, ilmenite,

620 quartz, sodic plagioclase, rutile and tourmaline (Gleizes, 1971; Thiébaut *et al.*, 1992). This
621 evaporitic material is found in a magnesian chlorite + illite rich matrix that hosts dolomite
622 layers associated with talc and ophite stocks plurihectometric in size. In Arignac-Bedeilhac,
623 north of the NPF, a similar situation is displayed by a Keuper epizonal brecciated formation
624 that again contains (meta-) evaporites (anhydrite and gypsum) and several phases also found
625 in the SBMS, notably: F- and Cl- rich apatite, chlorite, dolomite, magnesian hornblende,
626 phlogopite, rutile, scapolite, talc and tourmaline (Bouscary, 1966; Thiébaut *et al.*, 1988, 1992).
627 The latter authors emphasized the high Mg, Al, Na, Cl, F and B contents of these rocks. In the
628 western Pyrenees, Keuper epizonal cataclastic and metasomatized rocks are also described at
629 the interface between exhumed mantle, felsic continental crustal units and syn-rift Mesozoic
630 sediments in the Urdach and Saraillé massifs (Corre *et al.*, 2018; Lagabrielle *et al.*, 2019). They
631 form a boudinaged layer consisting of a mixture of polymineralic clasts (dolomite,
632 metasomatized felsic metamorphic rocks and micaschists, meta-ophites) embedded within a
633 schistose matrix of talc and Mg-chlorite (Corre *et al.*, 2018; Lagabrielle *et al.*, 2019). A
634 comparable epizonal Keuper formation is also known in the Basque-Cantabrian Basin
635 (DeFelipe *et al*., 2017).
636 Whether metasomatic alteration was responsible at least for part of the Al-Mg richness in the
637 SBMS prior to or during metamorphism is an open question. Indeed, the involvement of
638 metasomatic fluids is likely, considering reports from the western Pyrenees and the Basque-
639 Cantabrian Basin (Corre *et al*., 2018; DeFelipe *et al*., 2017; Salardon *et al*., 2017; Lagabrielle *et*
640 *al*., 2019). Derivation of Mg from the metasomatism of Mezosoic dolomitic sediments is
641 unlikely. Indeed, although carbonate formations are frequently dolomitic in the area of HT-LP
642 metamorphism of the NPZ (Fig. 1a), this is considered to reflect metasomatic Mg addition
643 which preceded talc formation. Such Mg addition was achieved through very high fluid-rock

644 ratios, as exemplified by the huge Trimouns talc deposit (Boulvais *et al*., 2006; Boutin *et al*.,
645 2016). Accordingly, the other possible source of Mg is the Keuper brines themselves.
646 All the geological markers around the Lherz sapphirine clastic deposits indicate that
647 they reside at the location of a major detachment capping the exhumed mantle. Accordingly,
648 we may assume that the original protolith(s) of the Lherz SBMS evolved in a detachment fault,
649 assisted by variable amount of fluids containing elements including Si, Mg, Fe, Ca, Cl, B, Sr, F.
650 Transformation of Triassic material along major detachment faults has already been
651 emphasized by Corre *et al.* (2018). The latter authors describe tectonic contacts between
652 mantle rocks and Mesozoic sediments characterized by the occurrence of Triassic cataclastic
653 material affected by intense syn-kinematic hydrothermal circulations. These contacts
654 represent the detachment faults along which subcontinental mantle was exhumed toward
655 upper crustal levels during the opening of the Albian-Cenomanian rift at the locus of the
656 future NPZ.

657 ## 4- P-T formation conditions of the Lherz SBMS protolith(s)

658 Calculating P and T formation conditions from the SBMS is problematic since: (i) the
659 SBMS, owing to its tectono-sedimentary nature, might derive either from a single protolith or
660 from a mixture of several protoliths; (ii) even in the case of a single protolith, the sapphirine-
661 bearing clasts are too small to identify the entire primary paragenesis and the whole-rock
662 chemistry that are needed for multi-equilibrium thermobarometry; (iii) thermodynamic data
663 for sapphirine remain highly uncertain (*cf.* Podlesskii *et al*., 2008; Wheller & Powell, 2014); (iv)
664 a contribution of evaporite-derived fluids is likely thus making the P-T calculation highly
665 dependent on reduced H_2O activity (Nijland *et al.*, 1998; Engvik & Austrheim, 2010).
666 Consequently, we will only attempt to fix bounds to the P-T estimates.

667 In the absence of corundum (or pyrope), a lower T limit is given by the extent of
668 Tschermak substitution in orthopyroxene, through the fluid-independent reaction enstatite +
669 corundum = $MgAl_2SiO_6$ ('Mg-Tschermak'). The 5-6 mol% Mg-Tschermak measured in
670 aluminous enstatite indicate a *minimum* T of about 550°C at low pressures and of ~600°C at
671 1.5 GPa (*e.g.* Gasparik, 1994), regardless of fluid presence or composition.
672 Another fluid-independent indication is given by the stability of anthophyllite (*vs*. talc +
673 enstatite in the MgO-SiO_2-H_2O system), which implies a *minimum* T varying from ~550 °C at
674 very low pressure to ~750°C at 1 GPa (Berman *et al*., 1986).
675 According to the inclusion and intergrowth relationships observed in the clasts, the
676 pairs enstatite–chlorite, sapphirine–anthophyllite and sapphirine–spinel were stable in the
677 source rock of the SBMS (Tab. 2, see also Fig. 5.1, 5.5, 5.6, 6.1 and 10.4). In the magnesian
678 system, the stability of sapphirine (+H_2O) combined with those of chlorite + enstatite and of
679 anthophyllite define a relatively narrow crescent in the P-T field, about 50°C wide in its
680 broadest part, concave toward the P axis and extending from about 600°C at very low P to
681 about 800°C near 1 GPa P_{H2O} (Seifert, 1974; Berman *et al*., 1986). However, all the reactions
682 involved are dehydration reactions and so the whole crescent may shift to lower
683 temperatures with decreasing H_2O activity.
684 Leaving aside the ultrahigh-temperature assemblages like sapphirine–quartz or spinel–
685 quartz (*e.g*. Wheller & Powell, 2014), crystallization of sapphirine-bearing assemblages in
686 silica-poor systems most commonly indicates facies conditions of amphibolite–granulite
687 boundary to granulitic, with temperatures ranging from 700°C to 900°C and pressures from
688 0.3 to 1.1 GPa (*e.g.* Ackermand *et al*., 1982; Windley *et al*., 1984; Christy, 1989; Vry &
689 Cartwright, 1994). For the closest natural assemblages to the SBMS found in the literature,
690 the P-T estimates are around 700 - 800°C and 0.35 - 1.0 GPa (Ackermand *et al*., 1982; Vry &

691 Cartwright, 1994). One should however bear in mind that, (i) in the magnesian system, from
692 about 0.03 to at least 0.7 GPa P_{H2O}, sapphirine (+H_2O) may form from chlorite + spinel +
693 corundum at temperatures between 600° and 750°C, depending on pressure (Seifert, 1974),
694 (ii) at any given pressure, chlorite dehydrates at a less than 50°C higher T than sapphirine
695 formation (Seifert, 1974), and (iii) in the presence of brines and/or lowered H_2O activity,
696 dehydration reactions (the sapphirine-forming ones in particular) occur at lower
697 temperatures, by as much as 120°C lower for H_2O activity reduced to 0.4 (*e.g.* Simon &
698 Chopin, 2001). Accordingly, and given the abundance of vermiculites which likely derive from
699 phlogopite or aspidolite, the best T estimate range for the development of the SBMS is 550-
700 700°C, for a maximum P of 1 GPa. If one then assumes that the enstatite–sapphirine pair was
701 stable in the source rock, the low Al-content of enstatite points to temperatures around 600-
702 650°C and pressures of a few kilobars (Fig. 4 in Gasparik, 1994). Furthermore, the instability of
703 the alternative assemblage cordierite–spinel implies a *minimum* P, decreasing at such
704 temperatures from ~0.3 GPa to ~0.1 GPa with decreasing H_2O activity (Podlesskii *et al.*, 2008,
705 his Fig. 7), which is definitely the case in the presence of metamorphic brines (*e.g*. Aranovich
706 & Newton, 1997).

707 The Lherz area is, together with the Boucheville basin, the place where the North
708 Pyrenean HT-LP Cretaceous metamorphism reached the highest temperatures (Golberg &
709 Leyreloup, 1990; Clerc *et al.*, 2015; Chelalou *et al.*, 2016). In the Aulus Basin, the highest peak
710 temperature has been so far estimated to a maximum of 625°C by RSCM in Liassic rocks
711 located 1.5 km to the south of the Lherz body, whereas peak temperatures around 550°C are
712 commonly obtained in Triassic (1 km to the south of the Lherz body) and Jurassic (300 m to
713 4.4 km from the Lherz body edges) metasediments (Clerc *et al.*, 2015). Hence, the SBMS
714 records metamorphic T conditions that equal or slightly exceed the highest values in the area.

In the context of extreme crustal thinning during the formation of the Aulus Basin (Lagabrielle *et al*., 2016), the maximum P conditions for the formation of the SBMS are directly linked to the initial thickness of the pre-rift (Triassic to Aptian) + syn-rift (Albian to Turonian) sedimentary pile above the exhumed mantle. Compilation of existing stratigraphic data at the scale of the entire NPZ suggests a maximum thickness around 6-8 km for that sedimentary pile (*e.g.* Debroas, 1978; Canérot & Delavaux, 1986; Canérot, 1991). Therefore, the combined experimental and thermodynamic data allowing for sapphirine formation in the 0.1 - 0.2 GPa range, especially at relatively 'low' T near 600 - 650°C and under reduced H_2O activity (Podlesskii *et al*., 2008), are consistent with the geological constraints.

C. Timing of the events experienced by the SBMS

The U-Pb dating of rutile, which provide an apparent Cenomanian age (see section IV.D.), must be confronted with mineralogical and textural features before being ascribed to the formation of the SBMS. Three *a priori* scenarii may be envisioned. (1) The dated rutile grains originate from a Variscan protolith which was brecciated and sedimented before the Cenomanian. This sediment was re-heated during the Cretaceous HT-LP metamorphic episode. (2) The protolith of samples BCOR 68a-b experienced a unique metamorphic episode that occurred during the Cretaceous and it was subsequently brecciated and sedimented at a shallow depth during the Upper Cretaceous. (3) Same history as (2) but brecciation and sedimentation occurred later, most likely during the Paleogene Pyrenean shortening and even more recently regarding sedimentation. We discard hypothesis (1) on the basis of three arguments. As mentioned previously, Variscan rocks with such mineralogy and compositions are unknown in the regional basement. Moreover, even though such rocks would be a very discrete component of that basement, it is quite impossible to imagine that the sediments contain only clasts issued from that component whilst common major minerals from the

739 Variscan crust, namely quartz and feldspars issued from granitoids and felsic metamorphic
740 rocks, are lacking (Tab. 2). Finally, hypothesis (1) is not consistent with the rock textures.
741 Closure temperature of the U-Pb system in rutile is strongly controlled by the grain size and
742 considered to be around 600°C for crystals with sizes ranging from 100 to 200 µm, although it
743 can be as low as *ca.* 400°C (Cherniak, 2000; Mezger *et al*., 1989; see also Meinhold, 2010;
744 Blackburn *et al.*, 2011). Such a temperature range is however compatible with the Cretaceous
745 metamorphic peak temperatures known in the Lherz area (Clerc *et al*., 2015), *i.e.* with
746 amphibolite facies. In such conditions, recrystallization of a sediment associating clasts of very
747 different size and compositions would induce characteristic textural features such as growth
748 of large clasts at the expense of minor similar ones at their contact, which is never observed.
749 Rather, all the observed textures argue for fracturing, disaggregation and dispersion of the
750 largest crystals (see section V.A.1). Accordingly, we consider that the *ca.* 100 Ma date does
751 not correspond to a resetting event. Hypothesis (3) is also difficult to reconcile with the fact
752 that none of the samples forming the SBMS display clasts deriving from the surrounding
753 Jurassic to Cretaceous formations of the Aulus Basin which fed however the volumetrically
754 very dominant Lherz breccias. On the opposite, hypothesis 2 fits U-Pb geochronological data
755 and the prevalence of ultramafic and Triassic clasts in the sapphirine-bearing breccias and
756 their systematic location in contact with ultramafic bodies. Accordingly, we conclude that
757 metamorphism and brecciation occurred during the Cretaceous rifting event. The timing of
758 sedimentation is however poorly constrained.
759
760 D. A possible model of emplacement of the sapphirine-bearing rocks
761 The sapphirine-bearing rocks are found only in a contact zone at the border of the
762 Lherz body and constitute the lowermost unit of the Lherz breccias. Therefore, according to

763 recent models of subcontinental mantle exhumation in the NPZ (*e.g.* Jammes *et al.*, 2009;
764 Lagabrielle *et al.*, 2016), they are good candidates to represent the basal portion of the
765 metamorphic sedimentary pile that came in tectonic contact with the exhumed peridotites
766 during the Cretaceous extensional event. The T estimates for the crystallization of the SBMS
767 material (550°C - 700°C, and more probably 600 - 650°C) as well as the U-Pb geochronological
768 data are consistent with a formation contemporaneous with the Pyrenean high T
769 metamorphic event, *i.e.* during the activity of the detachment fault which accommodated the
770 uplift of the peridotites beneath the opening Aulus Basin (Fig. 12).

771 In this study, we have reported numerous evidence for a dominant Keuper origin of
772 the material reworked in the sapphirine-bearing rocks. We also argued that the SBMS
773 protolith(s) derive from the metasomatic transformation of tectonized Keuper evaporitic
774 sediments under the influence of fluid circulations. Thus, we may speculate that the SBMS
775 protolith(s) originated along a major detachment fault at the final stages of the extreme
776 crustal thinning when the mantle rocks reached the base of the Mesozoic sedimentary pile,
777 under severe temperature conditions.

778 Our understanding of the Cretaceous mantle exhumation processes in the Pyrenees
779 lacks geological constraints and still remains incomplete. In this topic, our study provides the
780 following results: (i) the brecciated texture and the presence of unequivocal sedimentary
781 features in the sapphirine-bearing rocks show that the metasomatized Keuper material first
782 crossed the ductile-brittle transition and was then mechanically disaggregated before
783 experiencing some kind of winnowing in underwater conditions and (ii) we infer that these
784 rocks underwent minor spatial remobilization since their surface exposure, which is
785 consistent with the poor mixing observed between the different sources. Accordingly, the
786 most plausible scenario for the origin of the sapphirine-bearing rocks that integrates all our

observations is as follows: (i) the progressive exhumation of the extensional detachment and its footwall toward shallow levels induced the transition from ductile to brittle deformation responsible for the initial fracturing of the rocks and crystals; (ii) uplift was accompanied by progressive unroofing of deep levels of the detachment fault on the floor of the basin; (iii) exposure of the fault rocks allowed the reworking and primary sorting of the cataclastic material by gravity-driven processes. Determining whether these latter reworking processes occurred entirely during the exhumation event or somewhat later is beyond the scope of the present paper and needs a discussion of the whole system of the Lherz breccias, including the overwhelming carbonate-types.

In this scenario, the status of the sparitic calcite which forms the cement between the fragments and fills cracks within monomineralic clasts in Type II samples is equivocal. It might be a primary component (ophicalcitic cement, as exemplified by Denny *et al.*, 2016, or dolomitic component of Keuper sediments themselves), metamorphosed and subsequently redistributed, or it might have been introduced only during the brecciation stage like the calcitic cement of the Lherz breccias. Deciphering between these two hypotheses requires further investigation (*e.g.* RSCM, stable isotopes geochemistry).

VI. Conclusion

This detailed petrographic study of sapphirine-bearing rocks exposed in a contact zone between the Lherz mantle peridotites and the Lherz breccias reveals that some samples are composed of polymineralic clasts and isolated minerals that derive from well-recognized protoliths, mostly ultramafic rocks and Triassic meta-ophites and “micaceous hornfels”; however, a large portion of the sapphirine-bearing clastic suite is composed of mono- and polymineralic debris that derive from unknown protolith(s). We thus defined a "sapphirine-

bearing mineral suite" (SBMS) composed of monomineralic debris including: sapphirine + enstatite + aluminous spinel + Mg-amphiboles + Ca-amphiboles + kornerupine + accessory minerals (tourmaline, rutile, vermiculite and smectite).

The mineralogical study of the SBMS points to a peculiar Al-Mg-rich chemistry and reveals the presence of F-, Cl-, Sr-rich evaporitic inclusions in minerals of the Al-Mg-rich suite. This is consistent with a derivation of the SBMS from the metamorphic transformation of Keuper evaporitic sediments under high T and low P conditions, typical of the Cretaceous Pyrenean metamorphism. This contradicts the former interpretation of the Lherz sapphirine-bearing suite as crustal basement felsic rocks modified at depth along the contact with the ultramafic rocks of the Lherz body during their ascent towards shallower depths. Our hypothesis is also supported by the location of the sapphirine-bearing rocks at the precise contact zone between the exhumed Lherz body and the Lherz breccias.

According to recent models of subcontinental mantle exhumation in the NPZ (Lagabrielle & Bodinier, 2008; Clerc *et al.*, 2015; Lagabrielle *et al*., 2016), we propose that the sapphirine-bearing rocks represent the first formation deposited over the peridotites exposed on the floor of the Aulus Basin due to the activity of a detachment fault. The T estimates for the crystallization of the SBMS material (550°C - 700°C, and more probably 600 - 650°C) and U-Pb ages of *ca*. 100 Ma obtained on rutile are consistent with a formation contemporaneous with the Pyrenean HT metamorphic event, which is during the activity of the fault that accommodated the uplift of the peridotites beneath the opening Aulus Basin.

Field and microscopic observations imply that the sapphirine-bearing sandstones and breccias formed in a context of active tectonics allowing for the brecciation of a variety of lithological assemblages and their mechanical and sedimentary mixing. A scenario that integrates all our observations is as follows: (i) initial fracturing of the rocks and crystals due

to progressive uplift of the extensional detachment toward shallow levels crossing the transition from ductile to brittle deformation; (ii) progressive unroofing of deep levels of the detachment fault on the floor of the basin; (iii) exposure of the fault rocks followed by reworking and primary sorting of the cataclastic material by gravity-driven processes.

Acknowledgements

This work was supported by the UMR 6118 - Géosciences Rennes and by the RGF-Pyrénées project of the “Bureau de Recherches Géologiques et Minières” (BRGM, T. Baudin, manager). We warmly thank B. Azambre for his help on petrographic analysis and for fruitful discussions at Géosciences Rennes. We also thank M. Ducoux and an anonymous reviewer for their insightful comments which helped to improve the clarity of the manuscript.

References

Abraham K, Monchoux P, Roux L, Seifert F. 1977. Observations sur les exsolutions dans les orthoamphiboles des roches à sapphirine des Pyrénées. *Bulletin de la Société française de Minéralogie et Cristallographie* 100: 329-333.

Ackermand D, Herd RK, Windley BF. 1982. Chemographic relationships in sapphirine-bearing rocks of the Limpopo belt, Southern Africa, *Revista Brasileira de Geociencias* 12(1-3): 292-300.

Albarède F & Michard-Vitrac A. 1978. Age and significance of the north-pyrenean metamorphism. *Earth and Planetary Science Letters* 40: 327-332.

Avé Lallemant HG. 1968. Structural and petrofabric analysis of an "alpine-type" peridotite: the lherzolite of the French Pyrénées. *Leidse Geologische Mededelingen* 42: 1-57.

Aranovich LY & Newton RC. 1997. H_2O activity in concentrated KCl and KCl-NaCl solutions at high temperatures and pressures measured by the brucite-periclase equilibrium. *Contributions to Mineralogy and Petrology* 127(3): 261-271.

Arima M & Barnett RL. 1984. Sapphirine bearing granulites from the Sipiwesk Lake area of the late Archaean Pikwitonei granulite terrain, Manitoba, Canada. *Contributions to Mineralogy and Petrology* 88: 102-112.

Asti R, Lagabrielle Y, Fourcade S, Corre B, Monié P. 2019. How do continents deform during mantle exhumation? Insights from the northern Iberia inverted paleo-passive margin, western Pyrenees (France). *Tectonics* DOI: 10.1029/2018TC005428.

Azambre B, Rossy M, Lago M. 1987. Caractéristiques pétrologiques des dolérites tholéiitiques d'âge triasique (ophites) du domaine pyrénéen. *Bulletin de Minéralogie* 110: 379-396.

Berman RG, Engi M, Greenwood HJ, Brown, TH. 1986. Derivation of internally-consistent thermodynamic data by the technique of mathematical programming: a review with application the system MgO-SiO2-H2O. *Journal of Petrology* 27(6): 1331-1364.

Bixel F & Lucas C. 1987. Approche géodynamique du Permien et du Trias des Pyrénées dans le cadre du Sud-Ouest Européen. *Cuadernos de Geología Ibérica = Journal of Iberian Geology: an international publication of earth sciences* 11: 57-82.

Blackburn T, Bowring SA, Schoene B, Mahan K, Dudas F. 2011. U-Pb thermochronology: creating a temporal record of lithosphere thermal evolution. *Contributions to Mineralogy and Petrology* 162(3): 479-500.

Bodinier JL, Guiraud M, Fabriès J, Dostal J, Dupuy C. 1987. Petrogenesis of layered pyroxenites from the Lherz, Freychinede and Prades ultramafic bodies (Ariege, French Pyrenees). *Geochimica et Cosmochimica Acta* 51(2): 279-290.

Boillot G, Grimaud S, Mauffret A *et al*. 1980. Ocean-continent boundary off the Iberian margin: a serpentinite diapir west of the Galicia Bank. *Earth and Planetary Science Letters* 48(1): 23-34.

Boulvais P, De Parseval P, D'Hulst A, Paris P. 2006. Carbonate alteration associated with talc-chlorite mineralization in the eastern Pyrenees, with emphasis on the St. Barthelemy Massif. *Mineralogy and Petrology* 88(3-4): 499-526.

878 Boulvais P, Ruffet G, Cornichet J, Mermet M. 2007. Cretaceous albitization and dequartzification of Hercynian peraluminous granite in the
879 Salvezines Massif (French Pyrenees). *Lithos* 93: 89-106.

880 Boutin A, de Saint Blanquat M, Poujol M *et al.* 2016. Succession of Permian and Mesozoic metasomatic events in the eastern Pyrenees with
881 emphasis on the Trimouns talc-chlorite deposit. *International Journal of Earth Sciences* 105: 747–770.

882 Bouscary C. 1966. Les minéraux de métamorphisme du Trias de Bédeilhac (Ariège). *Bulletin de la Société d'Histoire Naturelle de Toulouse*
883 102(1-2): 286-291.

884 Briqueu L & Innocent C. 1993. Datation U/Pb sur zircon et géochimie isotopique Sr et Nd du volcanisme permien des Pyrénées occidentales
885 (Ossau et Anayet). *Comptes rendus de l'Académie des sciences. Série 2, Mécanique, Physique, Chimie, Sciences de l'univers, Sciences de la*
886 *Terre* 316(5): 623-628.

887 Canérot J. 1991. Comparative study of the eastern Iberides (Spain) and the western Pyrenees (France) Mesozoic basins. *Palaeogeography,*
888 *palaeoclimatology, palaeoecology*, 87(1-4): 1-28.

889 Canérot J & Delavaux F. 1986. Tectonique et sédimentation sur la marge nord-ibérique des chaînons béarnais (Pyrénées-béarnaises). Remise
890 en question de la signification des lherzolites du sommet de Saraillé. *Comptes rendus de l'Académie des sciences. Série 2, Mécanique,*
891 *Physique, Chimie, Sciences de l'univers, Sciences de la Terre* 302(15): 951-956.

892 Chelalou R, Nalpas T, Bousquet R *et al.* 2016. New sedimentological, structural and paleo-thermicity data in the Boucheville Basin (eastern
893 North Pyrenean Zone, France). *Comptes Rendus de Géoscience* 348(3-4): 312-321.

894 Cherniak D. 2000. Pb diffusion in rutile. *Contributions et Mineralogy and Petrology* 139: 198-207.

895 Chetouani K, Bodinier JL, Garrido CJ, Marchesi C, Amri I, Targuisti K. 2016. Spatial variability of pyroxenite layers in the Beni Bousera orogenic
896 peridotite (Morocco) and implications for their origin. *Comptes Rendus de Géoscience* 348(8): 619-629.

897 Chew DM, Petrus JA, Kamber BS. 2014. U–Pb LA–ICPMS dating using accessory mineral standards with variable common Pb. *Chemical*
898 *Geology* 363: 185–199.

899 Choukroune P. 1970. Contribution à l'étude structurale de la zone métamorphique nord-pyrénéenne ; Tectonique et métamorphisme des
900 formations secondaires de la forêt de Boucheville (Pyrénées orientales). *Bulletin du Bureau des Recherches Géologiques et Minières* 4: 46-63.

901 Choukroune P. 1973. La brèche de Lherz dite « d'explosion liée à la mise en place des lherzolites » est une brèche sédimentaire d'âge
902 Cénozoïque (Pyrénées ariégeoises). *Comptes Rendus de l'Académie des Sciences*, *Série D* 277: 2621-2624.

903 Choukroune P. 1976. Structure et évolution tectonique de la Zone Nord-Pyrénéenne : Analyse de la déformation dans une portion de chaîne
904 à schistosité subverticale. *Mémoires de la Société géologique de France* 127.

905 Christy AG. 1989. The stability of sapphirine + clinopyroxene: implications for phase relations in the CaO-MgO-Al2O3-SiO2 system under
906 deep-crustal and upper mantle conditions. *Contributions to Mineralogy and Petrology* 102: 422-428.

907 Clerc C, Lagabrielle Y, Neumaier M, Reynaud JY, de Saint Blanquat M. 2012. Exhumation of subcontinental mantle rocks: evidence from
908 ultramafic-bearing clastic deposits nearby the Lherz peridotite body, French Pyrenees. *Bulletin de la Société Géologique de France* 183(5):
909 443-459.

910 Clerc C, Boulvais P, Lagabrielle Y, de Saint Blanquat M. 2014. Ophicalcites from the northern Pyrenean belt: a field, petrographic and stable
911 isotope study. *International Journal of Earth Sciences* 1–23.

912 Clerc C & Lagabrielle Y. 2014. Thermal control on the modes of crustal thinning leading to mantle exhumation: Insights from the Cretaceous
913 Pyrenean hot paleomargins. *Tectonics* 33: 1340–1359.

914 Clerc C, Lahfid A, Monié P *et al.* 2015. High-temperature metamorphism during extreme thinning of the continental crust: a reappraisal of
915 the north Pyrenean paleo-passive margin. *Solid Earth Discuss*ions 6: 1-61.

916 Clerc C, Lagabrielle Y, Labaume P *et al.* 2016. Basement–Cover decoupling and progressive exhumation of metamorphic sediments at hot
917 rifted margin. Insights from the Northeastern Pyrenean analog. *Tectonophysics* 686: 82-97.

918 Conquéré F. 1978. Pétrologie des complexes ultramafiques de l'Ariège, Doctoral Dissertation, Université Pierre et Marie Curie, 333 p.

919 Corre B, Lagabrielle Y, Labaume P, Fourcade S, Clerc C, Ballèvre M. 2016. Deformation associated with mantle exhumation in a distal, hot
920 passive margin environment: New constraints from the Saraillé Massif (Chaînons Béarnais, North-Pyrenean Zone). *Comptes Rendus de*
921 *Géoscience* 348(3-4): 279-289.

922 Corre B, Boulvais P, Boiron MC, Lagabrielle Y, Marasi L, Clerc C. 2018. Fluid circulations in response to mantle exhumation at the passive
923 margin setting in the North Pyrenean Zone, France. *Mineralogy and Petrology* 112(5): 647-670.

924 Costa S & Maluski H. 1988. Use of the ^{40}Ar-^{39}Ar stepwise heating method for dating mylonite zones: An example from the St. Barthélémy
925 massif (Northern Pyrenees, France). *Chemical Geology: Isotope Geoscience section* 72(2): 127–144.

926 Dauteuil O & Ricou LE. 1989. Une circulation de fluides de haute-température à l'origine du métamorphisme crétacé nord-
927 pyrénéen. *Geodinamica Acta* 3(3): 237-249.

928 Debroas EJ. 1978. Evolution de la fosse du flysch ardoisier de l'Albien supérieur au Sénonien inferieur (zone interne métamorphique des
929 Pyrénées navarro-languedociennes). *Bulletin de la Société géologique de France* 7(5): 639-648.

930 Debroas EJ, Bilotte M, Canérot J, Astruc G. 2010. Réinterprétation des brèches de la Faille nord-pyrénéenne ariégeoise (France). *Bulletin de la*
931 *Société d'Histoire Naturelle de Toulouse* 146: 77-88.

932 DeFelipe I, Pedreira D, Pulgar JA, Iriarte E, Mendia M. 2017. Mantle exhumation and metamorphism in the Basque-Cantabrian Basin (N
933 Spain): Stable and clumped isotope analysis in carbonates and comparison with ophicalcites in the North-Pyrenean Zone (Urdach and Lherz).
934 *Geochemistry, Geophysics, Geosystems* 18(2): 631-652.

935 Denèle Y, Paquette JL, Olivier P, Barbey P. 2012. Permian granites in the Pyrenees: the Aya pluton (Basque Country). *Terra Nova* 24(2): 105-
936 113.

Denèle Y, Laumonier B, Paquette JL, Olivier P, Gleizes G, Barbey P. 2014. Timing of granite emplacement, crustal flow and gneiss dome formation in the Variscan segment of the Pyrenees. Geological Society, London, Special Publications 405(1): 265-287.

Denny AR, Kelley DS, Früh-Green GL. 2016. Geologic evolution of the Lost City hydrothermal field. *Geochemistry, Geophysics, Geosystems* 17(2): 375-394.

De Saint Blanquat M, Bajolet F, Grand'Homme A *et al.* 2016. Cretaceous mantle exhumation in the central Pyrenees: new constraints from the peridotites in eastern Ariège (North Pyrenean zone, France). *Comptes Rendus de Géoscience* 348(3-4): 268-278.

Ducoux M. 2017. Structure, thermicité et évolution géodynamique de la Zone Interne Métamorphique des Pyrénées, Doctoral Dissertation, Université d'Orléans, 643 p.

Duretz, T, Asti R, Lagabrielle Y, Brun JP, Jourdon A, Clerc C, Corre B. 2019. Numerical modelling of Cretaceous Pyrenean Rifting: The interaction between mantle exhumation and syn-rift salt tectonics. *Basin Research* DOI: 10.1111/bre.12389.

Engvik AK & Austrheim H. 2010. Formation of sapphirine and corundum in scapolitised and Mg-metasomatised gabbro. *Terra Nova* 22(3): 166-171.

Espurt N, Callot JP, Totterdell J, Struckmeyer H, Vially R. 2009. Interactions between continental breakup dynamics and large-scale delta system evolution: Insights from the Cretaceous Ceduna delta system, Bight Basin, Southern Australian margin. *Tectonics* 28(6).

Fabriès J, Lorand JP, Bodinier JL, Dupuy C. 1991. Evolution of the upper mantle beneath the Pyrenees: evidence from orogenic spinel lherzolite massifs. *Journal of Petrology* (2): 55-76.

Fallourd S, Poujol M, Boulvais P, Paquette JL, de Saint Blanquat M, Remy P. 2014. In situ LA-ICP-MS U-Pb titanite dating of Na-Ca metasomatism in orogenic belts: the North Pyrenean example. *International Journal of Earth Sciences* 103(3): 667-682.

García Senz J. 2002. Cuencas extensivas del Cretácico Inferior en los Pirineos centrales. Formación y subsecuente inversión. Universitat de Barcelona.

Garrido-Megías A. 1972. Síntesis geológica del Secundario y Terciario entre los ríos Cinca y Segre (Pirineo central de la vertiente surpirenaica, provincias de Huesca y Lérida). *Boletín Geológico y Minero de España* 83: 1-47.

Gasparik T. 1994. A petrogenetic grid for the system MgO-Al2O3-SiO2. *The Journal of Geology* 102(1): 97-109.

Gillard M, Manatschal G, Autin J. 2016. How can asymmetric detachment faults generate symmetric Ocean Continent Transitions? *Terra Nova* 28(1): 27-34.

Gleizes G. 1971. Etude géologique et minéralogique du Trias de Betchat et de Bonrepaux (Ariège), Thèse de troisième cycle, Université Paul-Sabatier - Toulouse III and Bureau des Recherches Géologiques et Minières, 121 p.

Golberg JM & Maluski H. 1988. Données nouvelles et mise au point sur l'âge du métamorphisme pyrénéen = Age of the Pyrenean metamorphism: new data and discussion. *Comptes Rendus de l'Académie des Sciences* 306(6): 429-435.

966 Golberg JM & Leyreloup AF. 1990. High temperature-low pressure Cretaceous metamorphism related to crustal thinning (Eastern North
967 Pyrenean Zone, France). *Contributions to Mineralogy and Petrology* 104: 194-207.

968 Gong Z, Langereis CG, Mullender TAT. 2008. The rotation of Iberia during the Aptian and the opening of the Bay of Biscay. *Earth and*
969 *Planetary Science Letters* 273: 80–93.

970 Grew ES. 1988. Kornerupine at the Sar e Sang, Afghanistan, whiteschist locality: Implications for tourmaline-kornerupine distribution in
971 metamorphic rocks. *American Mineralogist* 73(3-4): 345-357.

972 Grew ES, Chernosky JV, Werding G, Abraham K, Marquez N, Hinthorne JR. 1990. Chemistry of kornerupine and associated minerals, a wet
973 chemical, ion microprobe, and X-ray study emphasizing Li, Be, B and F contents. *Journal of Petrology* 31(5): 1025-1070.

974 Handy MR, Schmid SM, Bousquet R, Kissling E, Bernoulli D. 2010. Reconciling plate tectonic reconstructions of Alpine Tethys with the
975 geological–geophysical record of spreading and subduction in the Alps. *Earth-Science Rev*iews. 102: 121-158.

976 Harley SL. 1993. Sapphirine granulites from the Vestfold Hills, East Antarctica: geochemical and metamorphic evolution. *Antarctic*
977 *Science* 5(4): 389-402.

978 Harley SL & Motoyoshi Y. 2000. Al zoning in orthopyroxene in a sapphirine quartzite: evidence for >1120 °C UHT metamorphism in the
979 Napier Complex, Antarctica, and implications for the entropy of sapphirine. *Contributions to Mineralogy and Petrology* 138(4): 293-307.

980 Hawthorne FC, Cooper MA, Grew ES. 2009. The crystal chemistry of the kornerupite-prismatine series. III. Chemical relations. *Canadian*
981 *Mineralogist* 47: 275-296.

982 Henry P, Azambre B, Montigny R, Rossy M, Stevenson RK. 1998. Late mantle evolution of the Pyrenean sub-continental lithospheric mantle in
983 the light of new ^{40}Ar–^{39}Ar and Sm–Nd ages on pyroxenites and peridotites (Pyrenees, France). *Tectonophysics* 296(1-2): 103-123.

984 Jammes S, Manatschal G, Lavier L, Masini E. 2009. Tectonosedimentary evolution related to extreme crustal thinning ahead of a propagating
985 ocean: Example of the western Pyrenees. *Tectonics* 28(4).

986 Jöns N & Schenk V. 2008. Relics of the Mozambique Ocean in the central East African Orogen: evidence from the Vohibory Block of southern
987 Madagascar. *Journal of Metamorphic Geology* 26: 17-28.

988 Lacroix A. 1894. Les phénomènes de contact de la lherzolite et de quelques ophites des Pyrénées. *Bulletin du Service de la Carte Géologique*
989 *de France* 6: 307-346.

990 Lagabrielle Y & Bodinier JL. 2008. Submarine reworking of exhumed subcontinental mantle rocks: field evidence from the Lherz peridotites,
991 French Pyrenees. *Terra Nova* 20: 11-21.

992 Lagabrielle Y, Labaume P, de Saint Blanquat M. 2010. Mantle exhumation, crustal denudation, and gravity tectonics during Cretaceous rifting
993 in the Pyrenean realm (SW Europe): Insights from the geological setting of the lherzolite bodies. *Tectonics* 29(4).

994 Lagabrielle Y, Clerc C, Vauchez A *et al.* 2016. Very high geothermal gradient during mantle exhumation recorded in mylonitic marbles and
995 carbonate breccias from a Mesozoic Pyrenean paleomargin (Lherz area, North Pyrenean Zone, France). *Comptes Rendus de Géoscience* 348:
996 290-300.

997 Lagabrielle Y, Asti R, Fourcade S *et al.* 2019. Mantle exhumation at magma-poor passive continental margins. Part I. 3D architecture and
998 metasomatic evolution of a fossil exhumed mantle domain (Urdach lherzolite, north-western Pyrenees, France). *Bulletin de la Société*
999 *Géologique de France*, 190(1): 8.

1000 Lago M, Arranz E, Pocovi A, Galé C, Gil-Imaz, A. 2004. Permian magmatism and basin dynamics in the southern Pyrenees: a record of the
1001 transition from late Variscan transtension to early Alpine extension. *Geological Society, London, Special Publications* 223(1): 439-464.

1002 Le Roux V, Bodinier JL, Tommasi A *et al.* 2007. The Lherz spinel lherzolite: refertilized rather than pristine mantle. *Earth and Planetary Science*
1003 *Letters* 259(3): 599-612.

1004 Ludwig KR. 2001. Isoplot/Ex Version 2.49. A geochronological toolkit for Microsoft Excel. Berkeley Geochronology Center.

1005 Masini E, Manatschal G, Tugend J, Mohn G, Flament JM. 2014. The tectono-sedimentary evolution of a hyper-extended rift basin: the
1006 example of the Arzacq–Mauléon rift system (Western Pyrenees, SW France). *International Journal of Earth Sciences* 103(6): 1569-1596.

1007 McClay KR, Whitehouse PS, Dooley T, Richards M. 2004. 3D evolution of fold and thrust belts formed by oblique convergence. *Marine and*
1008 *Petroleum Geology* 21(7) : 857-877.

1009 Meinhold G. 2010. Rutile and its applications in earth sciences. *Earth-Science Reviews* 102(1-2): 1-28.

1010 Mezger K, Hanson GN, Bohlen SR. 1989. High precision U-Pb ages of metamorphic rutile: applaication to the cooling history of high-grade
1011 terranes. *Earth and Planetary Science Letters* 96: 106-118.

1012 Monchoux P. 1969. Corindon, kornerupine, sapphirine. *Bulletin de la Société française de Minéralogie et de Cristallographie* 92: 397-399.

1013 Monchoux P. 1970. Les lherzolites pyrénéennes : contribution à l'étude de leur minéralogie, de leur genèse et de leurs transformations.
1014 Doctoral Dissertation, Université de Toulouse, 180 p.

1015 Monchoux P. 1972a. Roches à sapphirine au contact des lherzolites pyrénéennes. *Contributions to Mineralogy and Petrology* 37: 47-64.

1016 Monchoux P. 1972b. Description des gisements de sapphirine associés aux lherzolites pyrénéennes : I. gisements de l'étang de Lherz. *Bulletin*
1017 *de la Société d'Histoire Naturelle de Toulouse*: 410-419.

1018 Montigny R, Azambre B, Rossy M, Thuizat R. 1986. K-Ar study of cretaceous magmatism and metamorphism in the Pyrenees: age and length
1019 of rotation of the Iberian Peninsula. *Tectonophysics* 129: 257-213.

1020 Moore, PB. 1969. The crystal structure of sapphirine. *American Mineralogist: Journal of Earth and Planetary Materials* 54(1-2): 31-49.

1021 Morishita T, Arai S, Gervilla F. 2001. High-pressure aluminous mafic rocks from the Ronda peridotite massif, southern Spain: significance of
1022 sapphirine-and corundum-bearing mineral assemblages. *Lithos* 57(2-3): 143-161.

1023 Nijland TG, Touret JL, Visser D. 1998. Anomalously low temperature orthopyroxene, spinel, and sapphirine occurrences in metasediments
1024 from the Bamble amphibolite-to-granulite facies transition zone (South Norway): possible evidence for localized action of saline fluids. *The*
1025 *Journal of Geology* 106(5): 575-590.

1026 Olivet JL. 1996. La cinématique de la plaque ibérique. *Bulletin des Centres de Recherche Exploration-Production Elf-Aquitaine* 20: 131-195.

1027 Paquette JL, Piro JL, Devidal JL *et al.* 2014. Sensitivity enhancement in LA-ICP-MS by N2 addition to carrier gas: Application to radiometric
1028 dating of U-Th-bearing minerals. *Agilent ICP-MS Journal* 58: 4-5.

1029 Paton C, Woodhead JD, Hellstrom JC, Hergt JM, Greig A, Maas R. 2010. Improved laser ablation U-Pb zircon geochronology through robust
1030 downhole fractionation correction. *Geochemistry, Geophysics, Geosystems* 11, Q0AA06.

1031 Péron-Pinvidic G & Manatschal G. 2009. The final rifting evolution at deep magma-poor passive margins from Iberia-Newfoundland: a new
1032 point of view. *International Journal of Earth Sciences* 98(7): 1581-1597.

1033 Péron-Pinvidic G & Osmundsen PT. 2016. Architecture of the distal and outer domains of the Mid-Norwegian rifted margin: Insights from the
1034 Rån-Gjallar ridges system. *Marine and Petroleum Geology* 77: 280-299.

1035 Podlesskii KK, Aranovitch LY, Gerya TV, Kosyakova NA. 2008. Sapphirine-bearing assemblages in the system $MgO–Al_2O_3–SiO_2$: a continuing
1036 ambiguity. *European Journal of Mineralogy* 20: 721-734.

1037 Podlesskii KK. 2010. Stability of Sapphirine-Bearing Mineral Assemblages in the System $FeO–MgO–Al_2O_3–SiO_2$ and Metamorphic P–T
1038 Parametres of Aluminous Granulites. *Petrology* 18: 350-368.

1039 Poujol M, Boulvais P, Kosler J. 2010. Regional-scale Cretaceous albitization in the Pyrenees: evidence from in situ U–Th–Pb dating of
1040 monazite, titanite and zircon. *Journal of the Geological Society of London* 167: 751-767.

1041 Ravier J. 1959. Le métamorphisme des terrains secondaires des Pyrénées. *Mémoires de la Société Géologique de France* 86, 250 p.

1042 Ravier J & Thiébaut J. 1982. Sur l'origine lagunaire des marbres et cornéennes mésozoïques du col d'Agnes (Ariège). *Comptes Rendus de*
1043 *l'Académie des Sciences* 294: 127-130.

1044 Rosenbaum G, Lister GS, Duboz C. 2002. Relative motions of Africa, Iberia and Europe during Alpine orogeny. *Tectonophysics* 359: 117-129.

1045 Roux L. 1977. L'évolution des roches du faciès granulite et le problème des ultramafitites dans le massif de Castillon (Ariège), Doctoral
1046 Dissertation, Université de Toulouse, 487 p.

1047 Saspiturry N, Razin P, Baudin T, Serrano O, Issautier B, Lasseur E *et al*. 2019. Symmetry vs. asymmetry of a hyper-thinned rift: Example of the
1048 Mauléon Basin (Western Pyrenees, France). *Marine and Petroleum Geology* 104: 86-105.

1049 Schärer U, Parseval PD, Polvé M, de Saint Blanquat M. 1999. Formation of the Trimouns talc-chlorite deposit (Pyrenees) from persistent
1050 hydrothermal activity between 112 and 97 Ma. *Terra Nova* 11(1): 30-37.

1051 Schreyer W & Abraham K. 1976. Three-stage metamorphic history of a whiteschist from Sar e Sang, Afghanistan, as part of a former
1052 evaporite deposit *Contributions to Mineralogy and Petrology* 59(2): 111-130.

1053 Sibuet JC, Srivastava S, Manatschal G. 2007. Exhumed mantle-forming transitional crust in the Newfoundland-Iberia rift and associated
1054 magnetic anomalies. *Journal of Geophysical Research* 112, B06105.

1055 Simon G & Chopin C. 2001. Enstatite–sapphirine crack-related assemblages in ultrahigh-pressure pyrope megablasts, Dora-Maira Massif,
1056 western Alps. *Contributions to Mineralogy and Petrology* 140: 422-440.

1057 Stacey JS, Kramers JD. 1975 Approximation of terrestrial lead isotope evolution by a two-stage model. *Earth and Planetary Science Letters* 26:
1058 207-221.

1059 Ternet Y, Colchen M, Debroas EJ *et al.* 1997. Notice explicative, Carte géologique de France (1/50 000), feuille 1086, Aulus-les-Bains, *BRGM*
1060 *éditions, Bureau des Recherches Géologiques et Minières, Orléans.*

1061 Thiébaut J, Debeaux M, Durand-Wackenheim C *et al.* 1988. Métamorphisme et halocinèse crétacés dans les évaporites de Betchat le long du
1062 chevauchement frontal nord-Pyrénéen (Haute-Garonne et Ariège, France). *Comptes rendus de l'Académie des sciences, Série 2* 307: 1535-
1063 1540.

1064 Thiébaut J, Durand-Wackenheim C, Debeaux M, Souquet P. 1992. Métamorphisme des évaporites triasiques du versant nord des Pyrénées
1065 centrales et occidentales. *Bulletin de la Société d'Histoire Naturelle de Toulouse* 128: 77-84.

1066 Tugend J, Manatschal G, Kusznir NJ, Masini E. 2015. Characterizing and identifying structural domains at rifted continental margins:
1067 application to the Bay of Biscay margins and its Western Pyrenean fossil remnants. *Geological Society, London, Special Publications* 413(1):
1068 171-203.

1069 Vauchez A, Clerc C, Bestani L *et al.* 2013. Preorogenic exhumation of the North Pyrenean Agly massif (Eastern Pyrenees-France). *Tectonics*
1070 32: 1-12.

1071 Vielzeuf D & Kornprobst J. 1984. Crustal splitting and the emplacement of Pyrenean lherzolites and granulites. *Earth Planetary Science*
1072 *Letters* 67(1): 87-96.

1073 Vry JK & Cartwright I. 1994. Sapphirine-kornerupine rocks from the Reynolds Range, central Australia: constraints on the uplift history of a
1074 Proterozoic low pressure terrain. *Contributions to Mineralogy and Petrology* 116(1-2): 78-91.

1075 Wheller CJ & Powell R. 2014. A new thermodynamic model for sapphirine: calculated phase equilibria in K_2O–FeO–MgO–Al_2O_3–SiO_2–H_2O–
1076 TiO_2–Fe_2O_3. *Journal of Metamorphic Geology* 32: 287-299.

1077 Whitney DL & Evans BW. 2010. Abbreviations for names of rock-forming minerals. *American Mineralogist* 95: 185-187.

1078 Windley BF, Ackermand D, Herd RK. 1984. Sapphirine/kornerupine-bearing rocks and crustal uplift history of the Limpopo belt, Southern
1079 Africa. *Contributions to Mineralogy and Petrology* 86(4): 342-358.

1080 Zack T, Stockli DF, Luvizotto GL *et al.* 2011. In situ U-Pb rutile dating by LA-ICP-MS: 208Pb correction and prospects for geological
1081 applications. *Contributions to Mineralogy and Petrology* 162(3): 515-530.

1083 Figure captions

1084 Figure 1: 1) Geological sketch map of the Pyrenees showing the location of the Lherz body.
1085 NPFT, North-Pyrenean Frontal Thrust; NPF, North-Pyrenean Fault; SPF, South-Pyrenean Fault;
1086 SPFT, South Pyrenean Frontal Thrust (modified after Corre *et al.*, 2016). 2) Geological map of
1087 the Aulus Basin (modified after Lagabrielle *et al*., 2016). Locations of the studied sites 1 and 2
1088 are indicated by red stars. Units of massive carbonates are separated by wide areas of
1089 polymictic sedimentary breccias. The ultramafic-bearing breccias are restricted to the central
1090 part of the Aulus Basin where the peridotite bodies are concentrated. Peak temperatures
1091 obtained by RSCM (Raman Spectroscopy of Carbonaceous Material) geothermometry on
1092 Mesozoic marble samples are from Clerc *et al*. (2015). Site 1: 42°48'30.52"N 1°22'52.85"E.
1093 Site 2: 42°48'26.78"N 1°23'7.97"E.

1094

1095 Figure 2: Field photographs from site 1. 1) Succession of clastic layers at site 1. Four layer
1096 types can be distinguished (see text for complete description). The dominant Layer A
1097 corresponds to light grey, coarse sandstones. Layer B corresponds to dark-brown layers of
1098 ultramafic breccias and microbreccias composed of dominant angular clasts of serpentinized
1099 lherzolite in an ultramafic sandy matrix. Layer C is represented by breccias and sandstones
1100 made of dominant ultramafic and minor cm-sized clasts of Triassic meta-ophite. Layer D is a
1101 coarse breccia composed of cm- to dm-sized angular clasts of ultramafic rock, white
1102 microbreccias, Triassic to Lower Jurassic meta-ophites and « micaceous hornfels ». 2) Sharp
1103 contact between Layer B ultramafic breccias (left) and light-grey Layer A sandstones (right). 3)
1104 Close up of gradded-bedding observed in Layer B microbreccias. 4) Detail view of Layer D
1105 breccia.

1106

Figure 3: Field photographs from site 2. 1) Photograph of the contact zone between the mantle peridotites and the Lherz breccias at site 2 and location of the sapphirine-bearing rocks sampling site (red star). White dotted lines underline the progressive transition existing between the Lherz body and the Lherz marble breccias. Around white dotted line n°1, a progressive transition from the sapphirine-bearing rocks to the pure marble breccias and microbreccias was observed. 2) Detailed view of the sampling site 2 and location of close up photographs 3 and 4 shown below. 3) Detailed view of the left side of exposure. It consists of a pale-green to light-grey microbreccia showing a rough bedding with layers of thin-grained sandstones dipping to the south-east (dashed lines). The microbreccia contains numerous cm-sized angular clasts of variable lithologies including “micaceous hornfels” and poorly serpentinized lherzolite (white outlines, determined on thin-sections). 4) Detailed view of the right side of exposure. Sandstones include numerous cm-sized angular clasts of variable compositions (white outlines). One black clast of meta-ophite is observed macroscopically (bottom right side of photograph).

1121 **Table 1:** Main features of the different rock-types which constitute the sample collection.
1122 Simplified sketches are provided for each rock-type, taking into account their main features.
1123 Different colours indicate different mineral species. *Abbreviations from Whitney & Evans*
1124 *(2010).*
1125
1126 **Table 2:** Mineralogy of the sample collection. *Abbreviations from Whitney & Evans (2010).*
1127
1128 **Figure 4:** Thin-section micrographs showing the main features of Type I samples. **1)**
1129 « Micaceous hornfels » clast. Note the poikiloblastic texture of the central scapolite, with
1130 numerous inclusions (plane-polarized light; sample BCOR 71). **2)** « Micaceous hornfels » clast.
1131 Note the tourmaline and anorthite inclusions in the central scapolite (plane-polarized light;
1132 sample BCOR 71). *Abbreviations from Whitney & Evans (2010).*
1133
1134 **Figure 5:** Representative micrographs of Type II samples. **1)** Representative example of the
1135 sapphirine-bearing microbreccias (cross-polarized light; sample BCOR 68a). Note the
1136 dominant highly fractured monomineralic clasts and the calcitic cement. One fractured
1137 polymineralic clast (sapphirine + gedrite) appears in the upper central part of the picture
1138 (redrawn in the inset). **2)** Plurimillimetric monomineralic clast of gedrite fragmented with very
1139 few displacements between the debris (cross-polarized light; sample BCOR 68a**. 3)** Sapphirine
1140 crystal showing corrosion gulfs infilled with calcite, surrounded by kinked vermiculite crystals
1141 displaying open cleavages (cross-polarized light; sample BCOR 68b). **4)** A highly fractured
1142 subhedral anthophyllite crystal, with calcite infill (plane-polarized light; sample BCOR 72). **5)**
1143 and **6)** Polymineralic clasts showing the intergrowth relationships between sapphirine and
1144 gedrite (cross-polarized light; sample BCOR 68a). *Abbreviations from Whitney & Evans (2010)*.

1145

1146 **Figure 6:** Representative micrographs of Type III samples**. 1)** Polymineralic clast of sapphirine
1147 + gedrite showing textural equilibrium between the two phases (redrawn in the inset; cross-
1148 polarized light; sample BCOR 72). Areas appearing in brown in the sapphirine crystal
1149 correspond to voids generated when the thin section was prepared. **2)** Millimetric subhedral
1150 kornerupine crystal displaying parallel-oriented rutile inclusions (plane-polarized light; sample
1151 BCOR 72). **3)** Peridotite clast. Yellow dotted lines underline the limits of the polymineralic clast
1152 (plane-polarized light; sample Momo 1). **4)** Meta-ophite clast underlined by a red dotted line.
1153 Two ultramafic clasts are underlined by yellow dotted lines (plane-polarized light; sample
1154 Momo 1). **5)** Polymictic sandstone exclusively made of monomineralic clasts. A coarse
1155 bedding is underlined by planar minerals (black dotted arrows parallel to the bedding; plane-
1156 polarized light; sample LHZ 49). **6)** Polymineralic clast of scapolitite (underlined by an orange
1157 dotted line) enclosed in a sandstone made of monomineralic clasts. Note the orientation of
1158 the vermiculite flakes, parallel to the borders of the scapolitite clast (plane-polarized light;
1159 sample BCOR 73). *Abbreviations from Whitney & Evans (2010).*

1160

1161 **Figure 7:** Evidence of mineral fragmentation. **1)** Highly fractured plurimillimetric crystal of
1162 anthophyllite (left side) disaggregated into small angular pieces that fed the microbreccia
1163 (cross-polarized light; sample LHZ 7a). **4)** line drawing of 3) highlighting the fragmentation of
1164 anthophyllite. *Abbreviations from Whitney & Evans (2010).*

1165

1166 **Figure 8:** Evidence of layering at macro-scale. The mineral content of each layer is given in the
1167 inset. Dominant elements in each layer are shown in bold. **1)** Photograph of NR 94 sample.
1168 Layering is defined by alternating bluish (a) and yellow-orange layers (b), characterized by

various grain sizes and by slightly different mineral compositions (*see Supplementary material SM2 for a complete description)*. **2)** Thin section photograph of sample Momo 1. A layering is underlined by red dotted lines.

Figure 9: Layering defined by overconcentration of minerals in BCOR 72 sample. **1)** Phase map (EDS analysis, elemental mapping). **2)** Surface percentage of each mineral species. * Undetermined, possibly weathered phases. ** Not observed in thin section.

Table 3: Representative analyses of the main phases of the SBMS. When several analyses are available for a mineral species, the average composition and the corresponding structural formula are given. For vermiculite and smectite, the structural formulae were not determined due to the great diversity of the microprobe analyses in our sample collection. *Average values are calculated on the basis of a) twelve analyses from four samples; b) twenty-nine analyses from two samples; c) seven analyses from three samples; d) five analyses from two samples; e) nine analyses from four samples; f) nineteen analyses from three samples; g) single analysis; h) three analyses from one sample; i) single analysis; j) five analyses from two samples; k) forty-six analyses from six samples; l) six analyses from two samples.*

Figure 10: Representative micrographs of the solid inclusions observed in minerals of the SBMS. **1)** Chlorapatite inclusion (outlined in blue) in a sapphirine crystal (reflected light; sample BCOR 68b). **2)** Anhydrite inclusion in a kornerupine crystal (Back-scattered electron image; sample BCOR 72). **3)** Coalescent anhydrite and chlorapatite inclusions in an Al-bearing enstatite crystal (cross-polarized light; sample NR 94). **4)** Clinochlore inclusions in aluminous

enstatite (plane-polarized light; sample NR 94, modified from F. Foucard, unpublished master thesis, Toulouse, 1997). *Abbreviations from Whitney & Evans (2010).*

Table 4: Electron-microprobe analyses of solid inclusions of evaporitic affinity in enstatite crystals from sample NR 94. *Average values of n analyses, with n= 6 for a), n= 3 for b), n= 5 for c).*

Table 5: LA-ICP-MS U-Pb isotope and age data for analyzed rutile grains in samples BCOR 72a-b. All errors are reported at 2σ. f206% = (207Pb/206Pbm - 207Pb/206Pb*)/(207Pb/206Pbc-207Pb/206Pb*)x100 with 207Pb/206Pb* and 207Pb/206Pbc calculated at 100 Ma.

Figure 11: Tera-Wasserburg concordia diagram for the U-Pb dating of rutile grains from samples BCOR68a-b. Error ellipses are plotted at 2σ. The lower intercept date of 98.6 ± 1.2 Ma is also reported with an error at 2σ.

Table 6: Bulk-rock analyses by Monchoux (1972a). 1, 2, 3: sapphirine-bearing rocks devoid of calcite, found at an increasing distance from the Lherz body. 4, 5: sapphirine-bearing rocks with calcite. *L.o.i.: Loss on ignition.*

Figure 12: Position of the main protolith of the SBMS suggested from this study in the Pyrenean rift (red star). The geometry of the rift is redrawn after Duretz *et al.* (2019). The P-T conditions of metamorphism of the Upper Jurassic to Lower Triassic protolith on contact with

1215 the asthenospheric mantle deduced from this study are given with their uncertainties in the

1216 inset.

1217

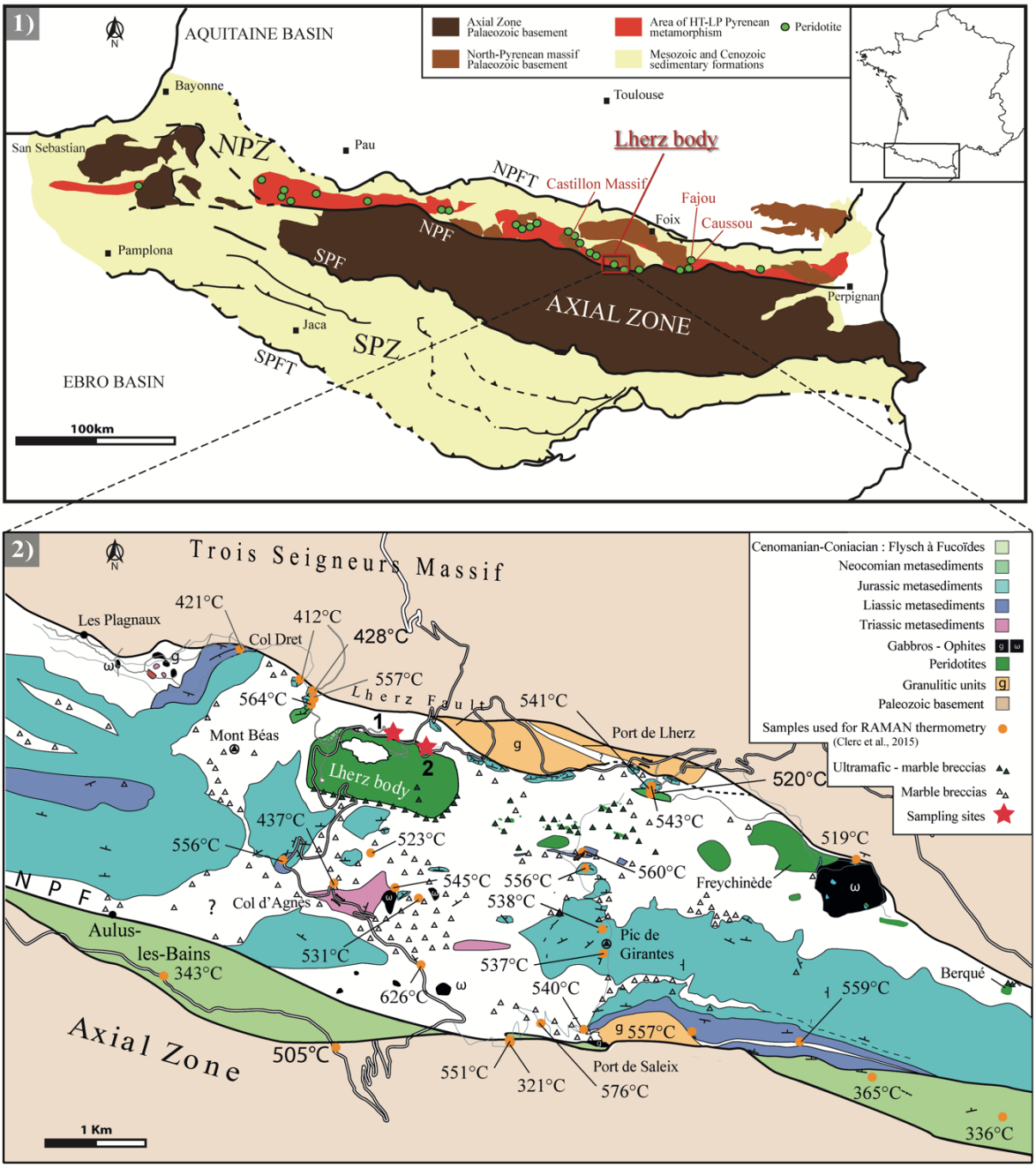

Figure 1 : 1) Schéma structural simplifié des Pyrénées montrant la localisation du corps de Lherz. NPFT, Chevauchement Frontal Nord-Pyrénéen ; NPF, Faille Nord Pyrénéenne ; SPFT, Chevauchement Frontal Sud-Pyrénéen (modifié d'après Corre *et al.*, 2016). **2)** Carte géologique du Bassin d'Aulus (modifiée d'après Lagabrielle *et al.*, 2016). Les étoiles rouges indiquent la localisation des sites 1 et 2 étudiés dans cet article. Les unités de carbonates massifs sont séparées les unes des autres par des brèches sédimentaires polygéniques. Les brèches à éléments ultramafiques sont observées au centre du Bassin d'Aulus, à proximité des corps de péridotite. Les temperatures obtenues par le géothermomètre RSCM (spectroscopie Raman de la matière carbonée) sur des échantillons de marbres mésozoïques sont tirées de Clerc *et al.* (2015).

Site 1 : 42°48'30.52"N 1°22'52.85"E. Site 2 : 42°48'26.78"N 1°23'7.97"E.

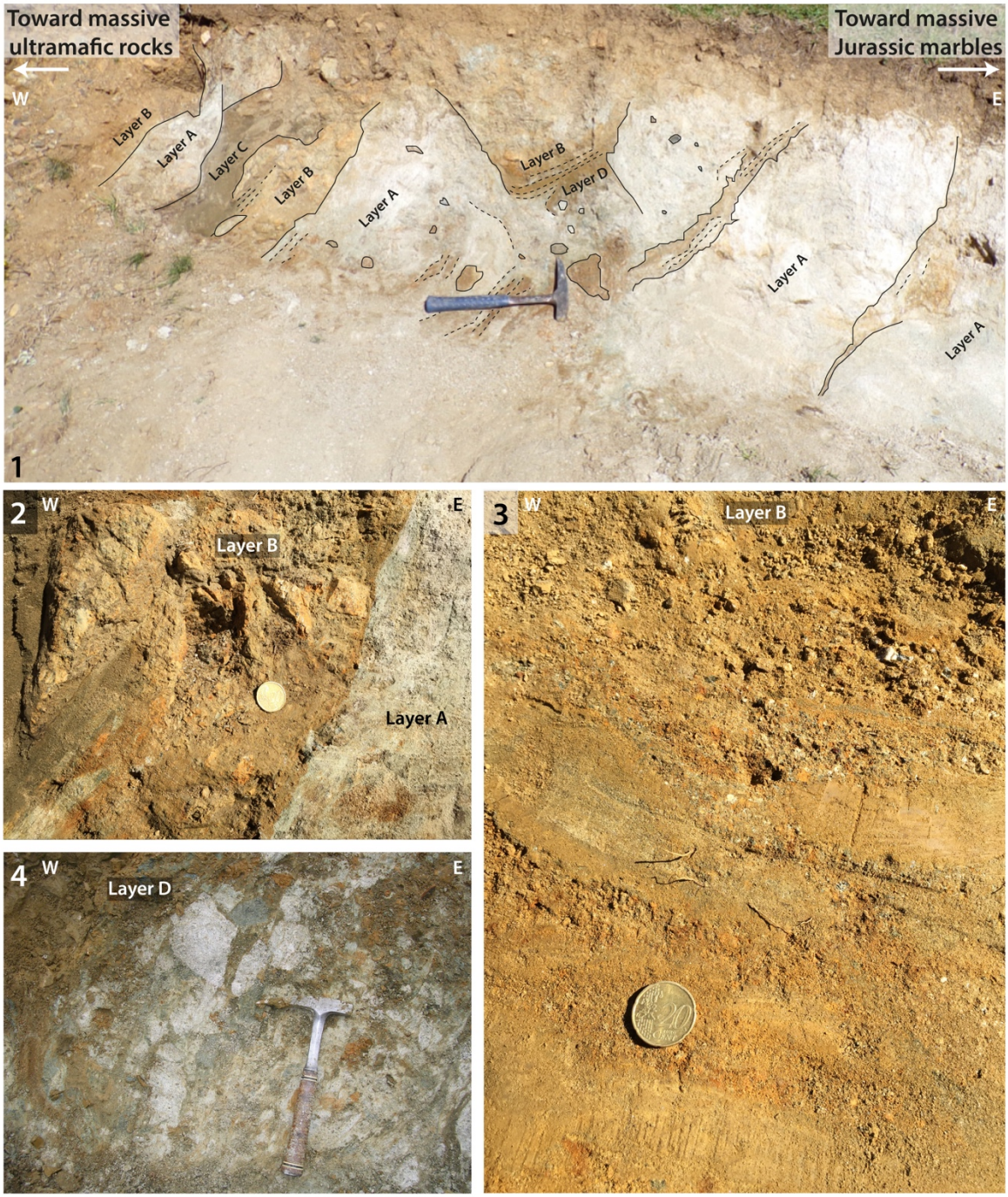

Figure 2 : Photographies réalisées sur le site 1. **1)** Succession des niveaux clastiques du site 1. Quatre types de niveau peuvent être distingués (se référer au texte pour une description complète). Le Lit A, dominant, correspond à un sable gris clair grossier. Le Lit B est constitué de niveaux marrons sombres de brèches et microbrèches ultramafiques, à clastes anguleux de lherzolite serpentinisée majoritaires dans une matrice ultramafique sableuse. Le Lit C correspond à des brèches et grès composés en majorité de clastes ultramafiques, et de plus rares clastes centimétriques de méta-ophites triasiques. Le Lit D est une brèche composée de clastes anguleux, de taille centimétrique à décimétrique, de roches ultramafiques, de microbrèches blanches, de méta-ophites et de « cornéennes micacées » triasiques à jurassiques inférieures. **2)** Contact franc entre les brèches ultramafiques du Lit B (à gauche) et les grès gris clairs du Lit A (à droite). **3)** Vue détaillée du granoclassement observé dans les microbrèches du Lit B. **4)** Vue détaillée de la brèche du Lit D.

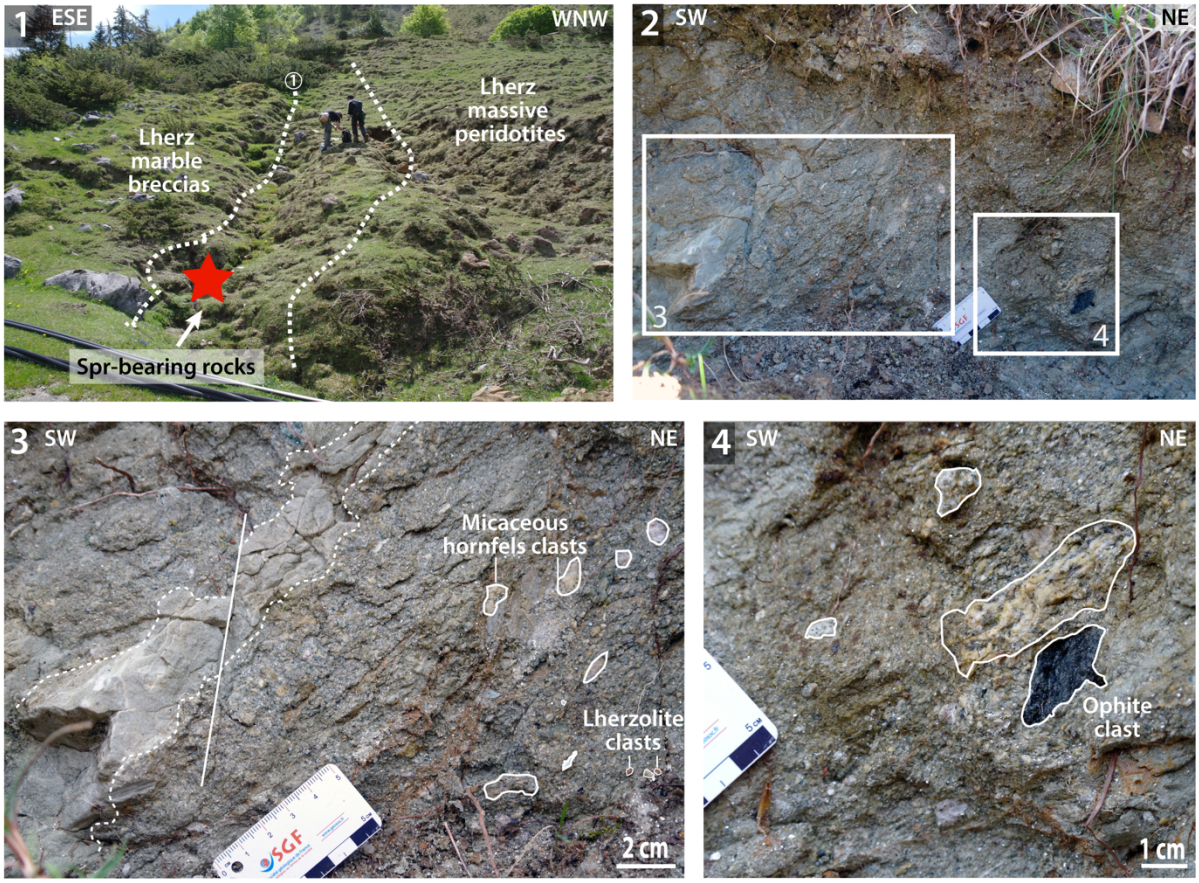

Figure 3 : Photographies du site 2. **1)** Photographie de la zone de contact entre les péridotites mantelliques et les brèches de Lherz au niveau du site 2. La localisation du site d'échantillonnage des roches à saphirine est représentée par l'étoile rouge. Les lignes blanches pointillées soulignent la transition progressive qui existe entre le corps de Lherz et les brèches de Lherz à clastes de marbres. A proximité de la ligne blanche pointillée n°1, nous avons observé une transition progressive entre les roches à saphirine et les brèches et microbrèches formées uniquement de clastes de marbre. **2)** Vue détaillée du site 2. La localisation des photographies 3 et 4 est représentée par les rectangles blancs. **3)** Vue détaillée d'une portion de l'affleurement. Cette portion correspond à une microbrèche de couleur vert pâle à grise claire et montre un litage formé de couches de grès fins à pendage vers le sud-est (lignes pointillées). La microbrèche contient en outre des clastes anguleux centimétriques de lithologies diverses incluant des « cornéennes micacées » et des lherzolites faiblement serpentinisées (entourées en blanc, reconnues en lame mince). **4)** Vue détaillée de la seconde portion de l'affleurement. Les grès contiennent de nombreux clastes anguleux centimétriques de compositions variables (entourés en blanc). Un claste noir méta-ophitique est observable macroscopiquement (partie inférieure droite de l'image).

Table 1 : Caractéristiques principales des différents types de roches de la collection d'échantillons étudiés dans cet article. Les schémas simplifiés se trouvant dans la dernière ligne du tableau mettent en avant les caractéristiques principales des différents types de roches. *Les abréviations utilisées sont tirées de Whitney & Evans (2010).*

Table 1 : Caractéristiques principales des différents types de roches de la collection d'échantillons étudiés dans cet article.

		Type I	Type II	Type III
Monomineralic clasts		Absence	Ultradominant	Ultradominant
Polymineralic clasts		Presence	Very scarce	Very scarce
Calcite in the cement		Absence	Presence	Absence
Protoliths		. Micaceous hornfels . Intermediate facies micaceous hornfels/marbles	. One or serveral unknown protoliths producing the SBMS	. Ultramafic rocks . Palaeozoic basement rocks . Intrusives . Micaceous hornfels . Sapphirine-bearing rocks
Sampling location				
Site 1	Layer A		*	*
	Layer B			*
	Layer C			*
	Layer D	*		
Site 2			*	
Simplified sketch		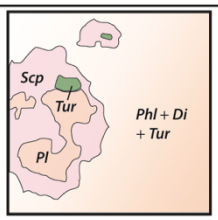	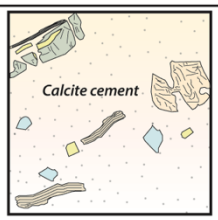	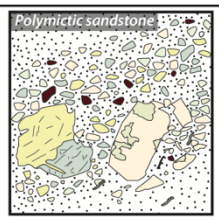

1265 **Table 2** : Minéralogie des échantillons étudiés dans cet article. *Les abréviations utilisées sont tirées de Whitney & Evans (2010).*

	Site	Layer type (at site 1)	Sample	Cement	Monomineralic clasts	Polymineralic clasts	Inclusions in minerals
Type I	Site 1	Layer D	BCOR 71	None	None	Di, Phl, Scp, Ep, Tur	Phl, Tur, Cl-Ap, An in Scp
			Momo 2			Di, Phl, Scp, Tur	Phl, Tur, Cl-Ap, An in Scp
			Momo 5			Di, Phl, Scp, An, K-Hs, Tur, Cal	
			Momo 6			Di, Phl, Scp, An, Zo	
Type II	Site 1	Layer A	Momo 2a	Cal	Ged, Prg, Vrm	None	
			Momo 2b		Al-Spl, Ap, Ged, Mg-Hb, Spr, Vrm	None	
			LHZ 7a		Al-Spl, Ca-Amp (Ts?), Ath, Rt, Spr, Tur, Vrm	None	
	Site 2		LHZ 114a		Di, Al-En, Ged, Prg, Spr, Srp, Vrm	None	
			BCOR 67b		Al-Sp, Cl-Ap, Rt, Spr, Sme, Vrm	Al-Spl, Spr	Ap in Spr
						Ath, Spr	Rt in Ath-Ged
			BCOR 68a		Ath-Ged, Rt, Spr, Sme, Vrm	Ath, Vrm	Cl-Ap, Rt in Spr
						Spr, Vrm	
						Ath, Spr, Vrm	
			BCOR 68b		Ath-Ged, Rt, Spr, Sme, Vrm	Spr, Vrm	Rt in Ath-Ged
						Ath, Spr, Vrm	Cl-Ap, Rt in Spr
			NR 94		Al-En, Al-Spl, Ap, Prg, Rt, Vrm	None	Anh, Ap, Clc, Zrn in Al-En
							Zrn, Cl-Ap in Prg
Type III	Site 1	Layer A	BCOR 72	None	Al-En, Di, Ged, Krn, Prg, Rt, Spr, Tur, Vrm, White mica	Ged, Spr	Rt in Ged
						Prg, Vrm	Rt, Ap, Anh in Krn
							Rt in Prg
		Layer B	Momo 1		Chl, Cpx, En, Cr-Hc, Mg-Hb, Ms, Phl, Pl, Qtz	En, Ol (8 Cr-Hc)	Green Hb, Ap in Pl
						Di, En	
						Mg-Hb, Pl 8 Cpx	
						En, Ol, Pl	
						Ms, Phl, Qz,	
			LHZ 49		Chl, Di, En, Hc, Cr-Hc, Ol, Ti-Prg, Qtz	None	
		Layer C	BCOR 73		Cpx, Prg, Rt, Scp, Green Spl, Tur, Vrm	Scp, Cpx, Vrm	

1266

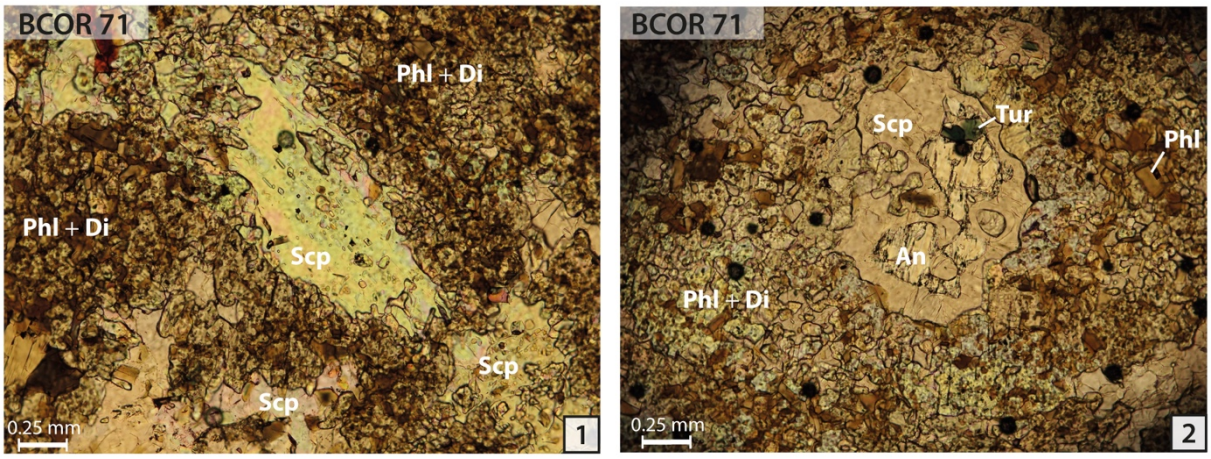

Figure 4 : Micrographies de lames minces montrant les principales caractéristiques des échantillons de Type I. **1)** Claste de « cornéenne micacée ». Noter la texture poeciloblastique de la scapolite centrale, qui contient de nombreuses inclusions (lumière polarisée non-analysée ; échantillon BCOR 71). **2)** Autre claste de « cornéenne micacée ». Noter les inclusions de tourmaline et d'anorthite dans la scapolite centrale (lumière polarisée non-analysée ; échantillon BCOR 71). *Les abréviations utilisées sont tirées de Whitney & Evans (2010).*

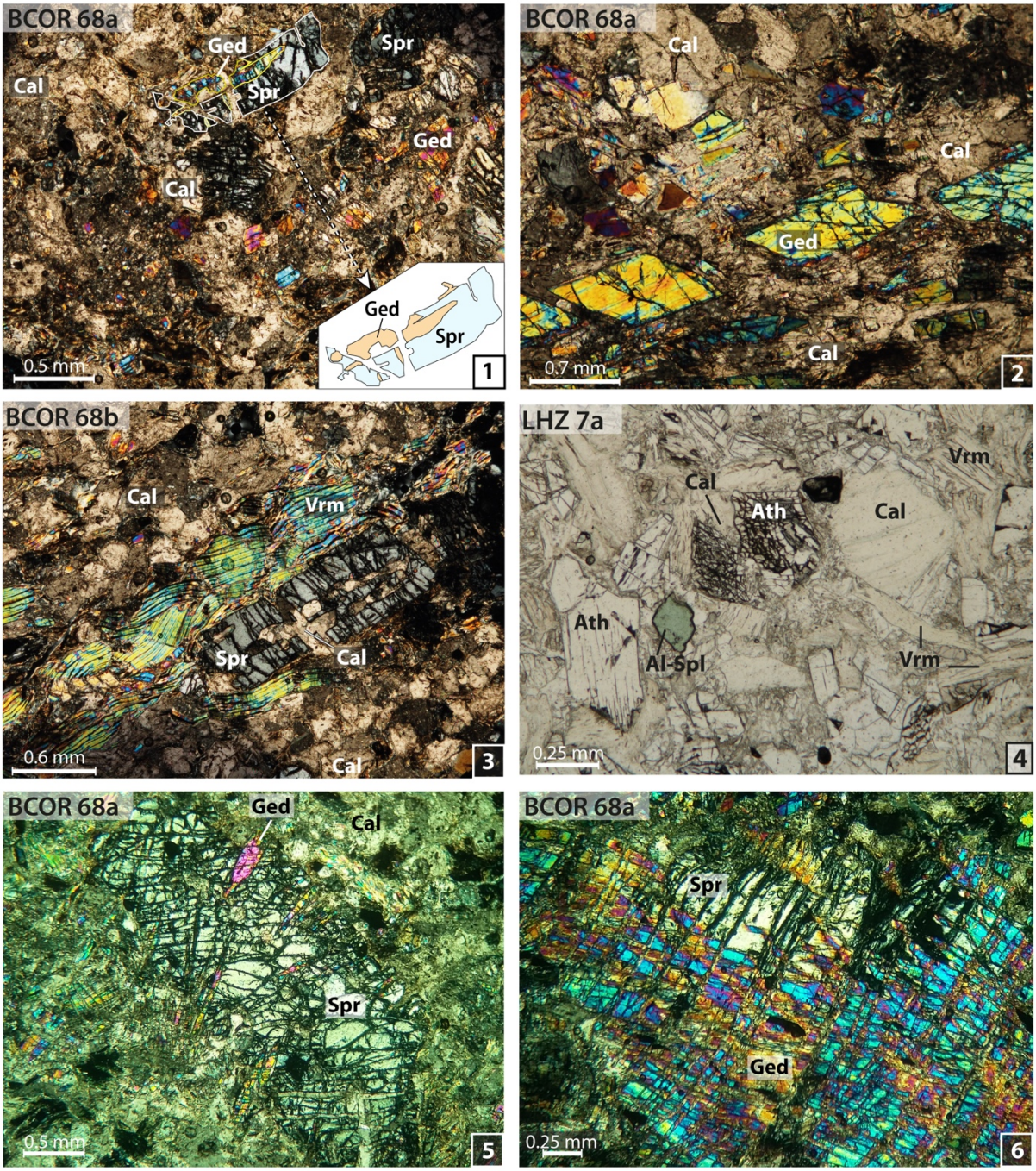

Figure 5 : Micrographies de lames minces montrant les principales caractéristiques des échantillons de Type II. **1)** Exemple représentatif des microbrèches à saphirine (lumière polarisée analysée ; échantillon BCOR 68a). Noter la prédominance des clastes monominéraux très fracturés et la présence d'un ciment calcitique. Un claste polyminéral (saphirine + gédrite) fracturé est présent dans la partie supérieure centrale de l'image (redessiné dans l'encart). **2)** Clastes monominéraux de gédrite, plurimillimétriques et fragmentés dont les débris sont peu éloignés les uns des autres (lumière polarisée analysée ; échantillon BCOR 68a). **3)** Cristal de saphirine à golfes de corrosion remplis de calcite, entourés de vermiculites kinkées à clivages ouverts (lumière polarisée analysée ; échantillon BCOR 68b). **4)** Cristal d'anthophyllite subautomorphe très fracturé et rempli de calcite. **5)** et **6)** Clastes polyminéraux montrant des intercroissances de saphirine et gédrite (lumière polarisée analysée ; échantillon BCOR 68a). *Les abréviations utilisées sont tirées de Whitney & Evans (2010).*

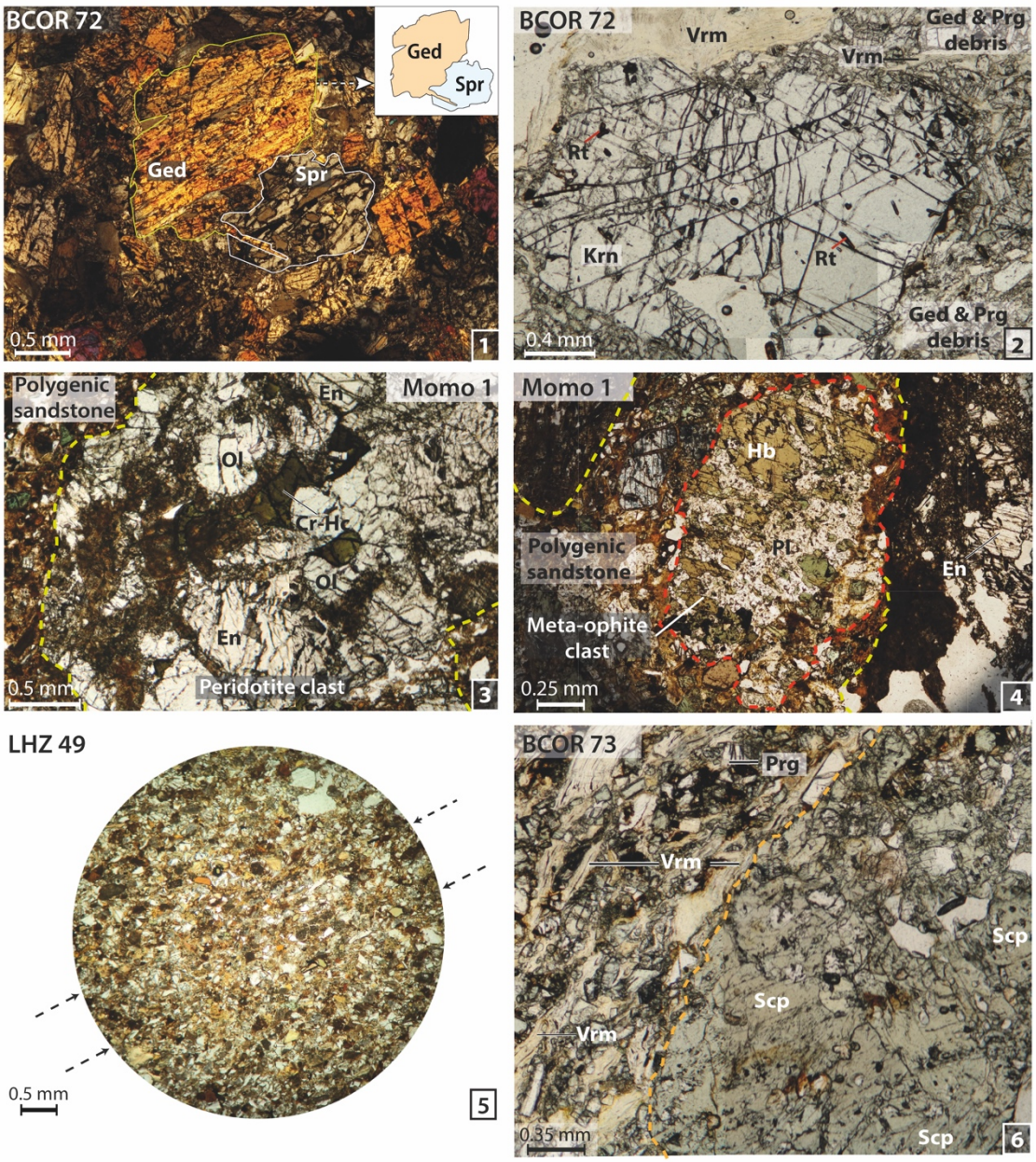

Figure 6 : Micrographies de lames minces montrant les principales caractéristiques des échantillons de Type III. **1)** Claste polyminéral à saphirine + gédrite en équilibre textural (redessiné dans l'encart ; lumière polarisée analysée ; échantillon BCOR 72). Les portions qui apparaissent en marron au sein de la saphirine correspondent à des vides générés au moment de la préparation de la lame mince. **2)** Cristal de kornérupine millimétrique subautomorphe à inclusions de rutile parallèles les unes aux autres (lumière polarisée non-analysée ; échantillon BCOR 72). **3)** Claste péridotitique. Les lignes pointillées jaunes soulignent les contours du claste ultramafique (lumière polarisée non-analysée ; échantillon Momo 1). **4)** Claste méta-ophitique (souligné par la ligne rouge pointillée). Deux clastes ultramafiques sont soulignés par les lignes jaunes pointillées (lumière polarisée non-analysée ; échantillon Momo 1). **5)** Grès polygénique constitué de clastes monominéraux. Un litage grossier est souligné par les minéraux planaires (l'orientation des flèches est parallèle au litage ; échantillon LHZ 49). **6)** Claste polyminéral de scapolitite (souligné par la ligne orange pointillée) dans un grès constitué de clastes monominéraux. Notez l'orientation des vermiculites, parallèles aux bordures du claste de scapolitite (lumière polarisée non-analysée ; échantillon BCOR 73). *Les abréviations utilisées sont tirées de Whitney & Evans (2010).*

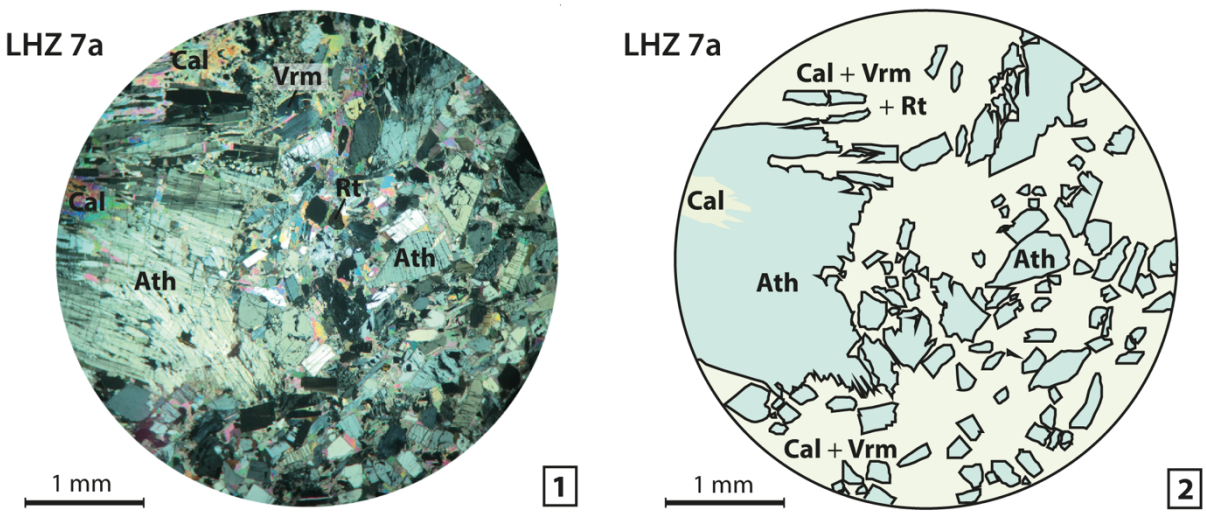

Figure 7 : Evidence de fragmentation des minéraux. 1) Cristal plurimillimétrique d'anthophyllite très fragmenté (gauche de l'image) et désagrégé en fragments de petite taille, constituant la microbrèche (lumière polarisée analysée ; échantillon LHZ 7a). 2) Esquisse de 1) soulignant la fragmentation de l'anthophyllite. *Les abréviations utilisées sont tirées de Whitney & Evans (2010).*

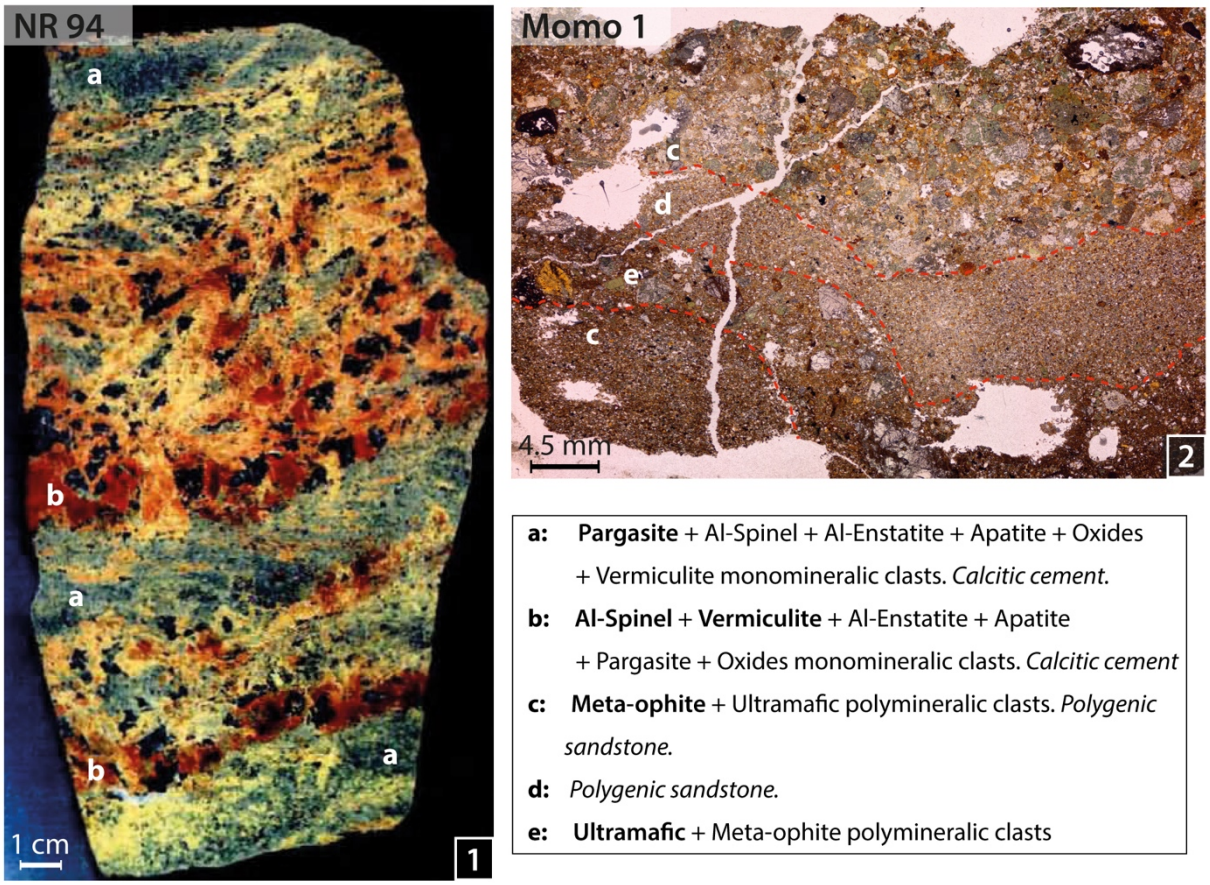

Figure 8 : Evidences de litage à l'échelle macroscopique. Les compositions des lits sont données dans l'encart. Les éléments dominants dans chaque couche sont figurés en gras. **1)** Photographie de l'échantillon NR 94. Un litage est défini par l'alternance de couches bleues (a) et oranges à jaunes (b) qui sont caractérisées par des tailles de grains variables et par des compositions légèrement différentes (*se référer aux ressources supplémentaires SM2 pour une description complète de l'échantillon*). **2)** Photographie de lame mince de l'échantillon Momo 1. Le litage est souligné par les lignes rouges pointillées.

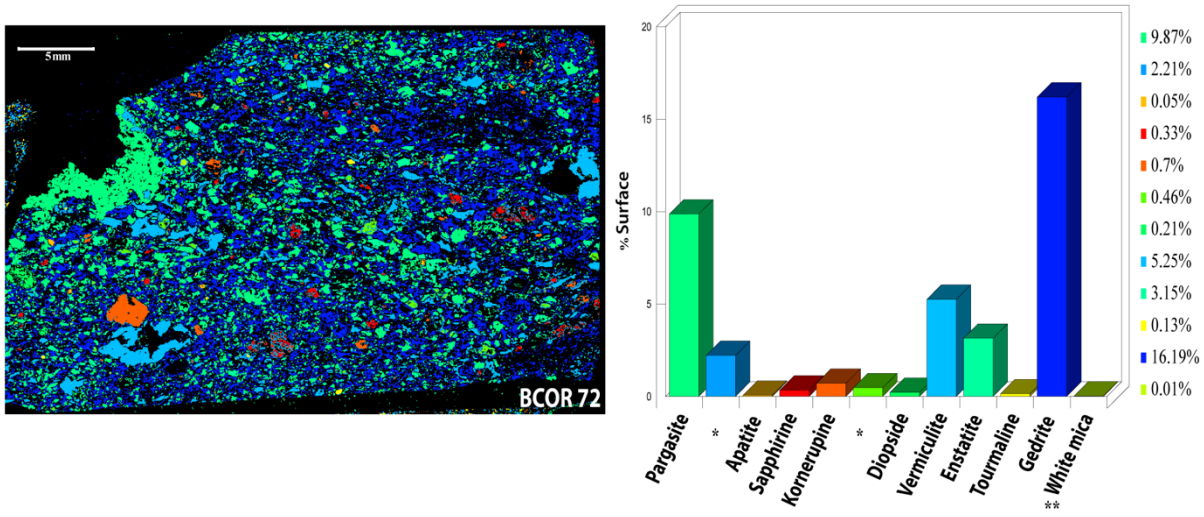

Figure 9 : Litage défini par l'accumulation de minéraux dans l'échantillon BCOR 72. **1)** Cartographie élémentaire de l'échantillon BCOR 72 (Carte des phases ; analyse dispersive en énergie). **2)** Pourcentage de la surface occupée par chaque espèce minérale dans l'échantillon. * Espèces non identifiées, potentiellement altérées. ** Non observé sur la lame mince.

Table 3 : Analyses représentatives des principales espèces de l'assemblage minéralogique à saphirine. Lorsque plusieurs analyses sont disponibles, une composition moyenne et la formule structurale correspondante sont calculées. Les formules structurales n'ont pas été calculées pour la vermiculite et la saponite du fait de l'importante diversité des analyses microsonde obtenues dans notre collection d'échantillons.

	Sapphirine		**Enstatite**		**Aluminous spinel**		**Mg-amphibole (anthophyllite)**	
	a	*Range*	b	*Range*	c	*Range*	d	*Range*
SiO_2	13.37	*12.79 – 13.7*	56.40	*55.49 – 57.29*	0.02	*0.00 - 0.06*	56.03	*55.51 – 56.91*
TiO_2	0.09	*0.02 – 0.13*	0.05	*0.00 – 0.11*	0.02	*0.00 – 0.07*	0,13	*0.08 – 0.18*
Al_2O_3	62.95	*59.49 – 64.85*	2.51	*1.89 – 3.48*	67.06	*65.10 – 68.65*	4.93	*4.90 – 5.25*
Cr_2O_3	0.04	*0.00 – 0.06*	--	--	0.08	*0.04 - 0.13*	0.00	*0.00 – 0.01*
FeO	3.87	*2.93 – 6.73*	6.77	*4.97 – 7.88*	10.32	*8.15 – 13.22*	6.18	*5.64 – 6.69*
MnO	0.01	*0.00 – 0.04*	0.08	*0.00 – 0.16*	0.02	*0.00 – 0.07*	0.02	*0.00 – 0.06*
MgO	19.44	*18.90 – 19.81*	33.94	*32.29 - 35.34*	22.33	*20.78 – 23.45*	29.24	*28.65 – 29.55*
CaO	0.04	*0.00 – 0.06*	0.14	*0.05 – 0.21*	0.04	*0.02 - 0.05*	0.59	*0.44 – 0.73*
Na_2O	0.01	*0.00 – 0.05*	0.04	*0.00 – 0.19*	0.00	*0.00 – 0.02*	0.47	*0.38 – 0.58*
K_2O	0.01	*0.00 – 0.02*	0.02	*0.00 – 0.05*	0.00	*0.00 – 0.01*	0.01	*0.00 – 0.02*
NiO	0.01	*0.00 – 0.02*	--	--	0.00	*0.00 – 0.01*	0.00	*0.00 – 0.00*
P_2O_5	0.02	*0.00 – 0.04*	--	--	0.00	*0.00 – 0.01*	0.01	*0.00 – 0.04*
Total	99.86		99.96		99.89		97.60	
Representative formulae								
Cations	**Basis of 20(O)**		**Basis of 6(O)**		**Basis of 4(O)**		**Basis of 23(O)**	
Si	1.58		1.95		0.00		7.52	
Ti	0.00		0.00		0.00		0.01	
Al	8.87		0.10		1.98		0.78	
Cr	0.00		0.00		0.00		0.00	
Fe^{3+}	0.00		0.00		0.00		0.17	
Fe^{2+}	0.30		0.20		0.17		0.52	
Mn	0.00		0.00		0.00		0.00	
Mg	3.42		1.75		0.85		5.85	
Ca	0.00		0.01		0.00		0.09	
Na	0.00		0.00		0.00		0.12	
K	0.00		0.00		0.00		0.00	
Total	14.18		4.00		3.01		15.06	
X_{Mg}	0.92		0.90		0.83		0.89	

Table 3 (suite) : *Les compositions moyennes sont calculées sur la base de a) douze analyses réalisées dans quatre échantillons ; b) vingt-neuf analyses dans deux échantillons ; c) sept analyses dans trois échantillons ; d) cinq analyses dans deux échantillons ; e) neuf analyses dans quatre échantillons ; f) dix-neuf analyses dans trois échantillons ; g) une seule analyse ; h) trois analyses dans un échantillon ; i) une seule analyse ; j) cinq analyses dans deux échantillons ; k) quarante-six analyses dans six échantillons ; l) six analyses dans deux échantillons.*

	Mg-amphibole (gedrite)		Ca-amphibole (pargasite)		Ca-amphibole (tschermakite?)	Kornerupine		Tourmaline
	e	*Range*	f	*Range*	g	h	*Range*	i
SiO_2	48.87	*43.50 – 52.3*	45.11	*42.61 – 48.92*	46.19	30.60	*30.22 – 31.08*	36.08
TiO_2	0.33	*0.23 – 0.59*	0.95	*0.76 – 1.31*	0.58	0.06	*0.05 – 0.09*	1.00
Al_2O_3	14.58	*10.35 – 21.39*	13.69	*10.21 – 16.01*	11.98	41.53	*40.43 – 42.78*	30.42
Cr_2O_3	0.01	*0.00 – 0.03*	--	--	0.00	0.04	*0.03 – 0.05*	0.01
FeO	4.80	*4.04 – 5.18*	3.25	*3.04 – 3.44*	4.80	2.97	*2.61 – 3.17*	2.41
MnO	0.03	*0.00 – 0.08*	0.01	*0.00 – 0.04*	0.05	0.00	*0.00 – 0.00*	0.02
MgO	26.69	*24.95 – 27.65*	18.81	*17.90 – 19.96*	18.44	19.81	*19.67 – 20.04*	11.17
CaO	0.84	*0.51 – 1.08*	12.22	*11.71 – 12.65*	12.62	0.07	*0.02 – 0.13*	3.08
Na_2O	1.49	*0.57 – 3.06*	2.31	*1.35 – 2.99*	1.55	0.06	*0.05 – 0.07*	1.13
K_2O	0.00	*0.00 - 0.01*	0.23	*0.19 – 0.26*	0.23	0.00	*0.00 – 0.01*	0.02
NiO	0.02	*0.00 – 0.05*	--	--	0.00	0.08	*0.03 – 0.13*	0.00
P_2O_5	0.01	*0.00 – 0.03*	--	--	0.02	--	--	0.00
B_2O_3	--	--	--	--	--	3.00	*2.78 – 3.28*	--
Total	97.67		96.58		96.45	98.22		85.35
Representative formulae								
Cations	**Basis of 23(O)**		**Basis of 23(O)**		**Basis of 23(O)**	**Basis of 21.5(O)**		**Basis of 24.5(O)**
Si	6.60		6.36		6.53	3.77		5.87
Ti	0.03		0.10		0.06	0.01		0.12
Al	2.32		2.28		2.00	6.02		5.84
Cr	0.00		0.00		0.00	0.00		0.00
Fe^{3+}	0.05		0.30		0.46	0.00		0.00
Fe^{2+}	0.50		0.09		0.11	0.31		0.33
Mn	0.00		0.00		0.01	0.00		0.00
Mg	5.36		3.95		3.88	3.63		2.71
Ca	0.12		1.85		1.91	0.01		0.54
Na	0.39		0.63		0.43	0.01		0.36
K	0		0,041		0,041	0		0,05
B	--		--		--	0,64		--
Total	15,38		15,59		15,42	14,40*		15,77
X_{Mg}	0,91		0,91		0,87	0,92		0,89

Table 3 (suite).

	Rutile		Vermiculite		Smectite	
	j	*Range*	k	*Range*	l	*Range*
SiO_2	0.01	*0.00 - 0.03*	35.81	*32.74 – 39.74*	47.84	*45.73 – 50.57*
TiO_2	99.69	*98.23 – 100.27*	0.98	*0.49 – 1.64*	0.05	*0.01 – 0.07*
Al_2O_3	0.06	*0.02 - 0.09*	16.51	*14.15 – 22.08*	8.49	*7.63 – 9.62*
Cr_2O_3	0.05	*0.01 - 0.09*	0.01	*0.00 – 0.03*	0.03	*0.00 – 0.06*
FeO	0.41	*0.37 - 0.47*	2.55	*1.63 – 6.06*	6.45	*4.65 – 7.91*
MnO	0.00	*0.00 – 0.01*	0.01	*0.00 – 0.09*	0.01	*0.00 – 0.02*
MgO	0.02	*0.00 – 0.04*	24.12	*21.72 – 30.88*	14.70	*11.62 – 16.41*
CaO	0.03	*0.00 – 0.08*	1.12	*0.26 – 2.89*	1.02	*0.53 – 1.49*
Na_2O	0.00	*0.00 – 0.02*	0.24	*0.00 – 0.57*	0.02	*0.00 – 0.04*
K_2O	0.00	*0.00 – 0.00*	0.42	*0.02 – 1.46*	0.10	*0.03 – 0.22*
NiO	0.00	*0.00 – 0.00*	0.01	*0.00 – 0.1*	0.04	*0.00 – 0.09*
P_2O_5	0.01	*0.00 – 0.02*	0.01	*0.00 – 0.04*	0.03	*0.00 – 0.08*
Total	100.28		81.79		78.78	

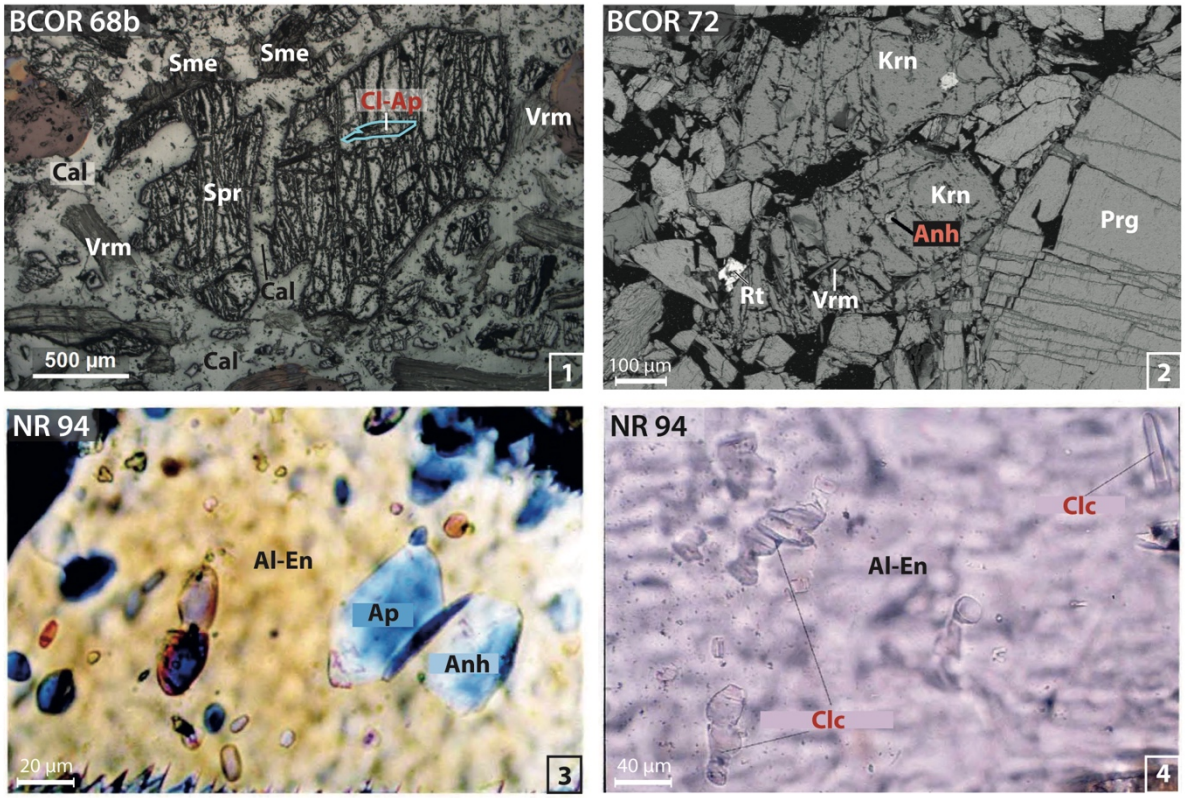

Figure 10 : Micrographies représentatives des inclusions solides observées dans les espèces minérales de l'assemblage minéralogique à saphirine. **1)** Inclusion de chlorapatite (soulignée en bleu) dans un cristal de saphirine (lumière réfléchie ; échantillon BCOR 68b). **2)** Inclusion d'anhydrite au sein d'un cristal de kornérupine (image en électrons rétrodiffusés ; échantillon BCOR 72). **3)** Inclusions coalescentes d'anhydrite et de chlorapatite au sein d'un cristal d'enstatite alumineuse (lumière polarisée analysée ; échantillon NR 94, modifié de F. Foucard, mémoire de master non publié, Toulouse, 1997). **4)** Inclusions de clinochlore dans une enstatite alumineuse (lumière polarisée analysée ; échantillon NR 94, modifié de F. Foucard, mémoire de master non publié, Toulouse, 1997). *Les abréviations utilisées sont tirées de Whitney & Evans (2010).*

Table 4 : Analyses microsonde des inclusions solides d'affinité évaporitique observées dans les cristaux d'enstatite de l'échantillon NR94. *Moyenne de n analyses avec n=6 pour a), n=3 pour b), n=5 pour c).*

	Anhydrite		Apatite		Clinochlore	
	a	*Range*	b	*Range*	c	*Range*
SiO_2	0.10	*0.06 – 0.12*	0.07	*0.02 – 0.13*	30.21	*29.95 – 30.45*
TiO_2	--	--	--	--	0.12	*0.07 – 0.17*
Al_2O_3	--	--	--	--	20.23	*20.01 – 20.46*
FeO	0.20	*0.10 – 0.32*	0.29	*0.21 – 0.33*	3.37	*3.21 – 3.47*
MnO	0.00	*0.00 – 0.00*	0.02	*0.00 - 0.05*	0.03	*0.00 – 0.06*
MgO	--	--	0.08	*0.00 – 0.13*	31.47	*31.08 – 31.88*
CaO	40.67	*40.33 – 41.31*	54.89	*54.25 – 55.44*	0.05	*0.01 - 0.11*
Na_2O	0.06	*0.00 – 0.18*	0.06	*0.02 - 0.08*	0.08	*0.02 - 0.16*
K_2O	0.03	*0.00 – 0.07*	--	--	0.13	*0.04 - 0.24*
NiO	--	--	--	--	0.04	*0.00 – 0.07*
SrO	0.42	*0.30 – 0.49*	--	--	--	--
SO_3	58.62	*57.34 – 59.59*	--	--	--	--
P_2O_5	--	--	40.23	*39.43 – 41.11*	--	--
La_2O_3	--	--	0.08	*0.00 – 0.19*	--	--
Ce_2O_3	--	--	0.04	*0.00 – 0.06*	--	--
F	--	--	2.02	*1.96 – 2.09*	--	--
Cl	--	--	1.93	*1.78 – 2.15*	--	--
$H_2O(c)$	--	--	0.28	*0.25 - 0.33*	--	--
O=F	--	--	0.85	*0.82 - 0.88*	--	--
O=Cl	--	--	0.43	*0.40 – 0.48*	--	--
Total	100.09		98.70		85.73	
Representative formulae						
Cations	Basis of 4(O)		Basis of 13(O, OH, F, Cl)		Basis of 14(O)	
Si	0.00		0.01		2.89	
Ti	--		--		0.01	
Al	--		--		2.28	
Fe^{3+}	0.00		--		0.00	
Fe^{2+}			0.02		0.27	
Mn	0.00		0.00		0.02	
Mg	--		0.01		4.49	
Ca	0.99		5.09		0.01	
Na	0.00		0.01		0.02	
K	0.00		--		0.02	
Sr	0.01		--		--	
S	1.00		--		--	
P	--		2.94		--	
La	--		0.00		--	
Ce	--		0.00		--	
F	--		0.55		--	
Cl	--		0.28		--	
OH	--		0.16		--	
Total	2.00		9.08		9.98	
X_{Mg}					0.94	

Table 5 : Données isotopiques et géochronologiques issues de l'analyse LA-ICP-MS des grains de rutile des échantillons BCOR 72a-b. Les erreurs sont reportées à 2σ. *f*206% = (207Pb/206Pbm - 207Pb/206Pb*)/(207Pb/206Pbc-207Pb/206Pb*)x100 avec 207Pb/206Pb* et 207Pb/206Pbc calculés à 100 Ma.

Rutile Grain	Analyses Number	U (ppm)	Pb (ppm)	*f*206%	Final238/206	PropErr%2Sig	Final207_206	PropErr%2Sig	207Pb-corrected date	PropErAbs2Sig
Rutile_1a	S-220216b-7	117	43	0.2	63.7	1.7	0.0495	3.2	100	2
Rutile_1b	S-220216b-8	109	65	0.0	65.1	2.8	0.0478	3.1	98	2
Rutile_4a	S-220216b-12	87	66	0.7	65.6	1.8	0.0539	3.7	97	2
Rutile_4b	S-220216b-18	139	143	1.1	63.5	1.8	0.0564	2.8	100	2
Rutile_6a	S-220216b-21	107	16	0.4	64.6	1.7	0.0510	3.9	99	2
Rutile_6b	S-220216b-22	107	27	0.7	62.8	1.7	0.0532	3.6	101	2
Rutile_6c	S-220216b-23	117	79	1.0	64.6	1.7	0.0560	3.4	98	2
Rutile_8a	S-220216b-30	107	137	0.6	63.3	1.7	0.0527	3.8	101	2
Rutile_8b	S-220216b-31	99	101	1.1	63.4	1.8	0.0565	3.4	100	2
Rutile_9a	S-220216b-32	109	441	2.3	63.3	3.0	0.0664	7.8	99	3
Rutile_9b	S-220216b-33	58	252	1.7	62.9	2.2	0.0617	5.7	100	2
Rutile_10a	S-301018a-1	142	19	0.6	64.0	5.6	0.0530	3.4	99	6
Rutile_10b	S-301018a-2	144	68	1.6	61.8	5.7	0.0605	3.1	102	6
Rutile_10c	S-301018a-3	124	86	1.6	61.7	5.9	0.0609	3.8	102	6
Rutile_11a	S-301018a-4	134	5	0.2	66.6	5.7	0.0494	4.0	96	6
Rutile_11b	S-301018a-5	147	35	0.2	66.5	5.6	0.0494	3.8	96	6
Rutile_11c	S-301018a-6	149	32	0.7	66.5	6.1	0.0538	4.3	96	6
Rutile_11d	S-301018a-7	111	16	0.5	68.9	5.7	0.0516	4.5	93	6
Rutile_11e	S-301018a-8	74	89	2.7	62.7	5.8	0.0694	5.9	99	7
Rutile_12a	S-301018a-9	164	3	0.1	65.7	5.7	0.0486	3.3	97	6
Rutile_12b	S-301018a-10	155	1	0.1	66.7	5.7	0.0490	3.3	96	6
Rutile_13a	S-301018a-11	144	10	0.4	66.5	5.7	0.0513	3.5	96	6
Rutile_13b	S-301018a-12	129	3	0.3	66.7	5.7	0.0503	3.6	96	6
Rutile_13c	S-301018a-13	143	27	0.5	65.7	5.8	0.0520	5.2	97	6
Rutile_14a	S-301018a-14	124	5	0.2	65.6	5.8	0.0495	3.8	98	6
Rutile_14b	S-301018a-15	119	7	0.0	65.2	5.7	0.0477	3.6	98	6

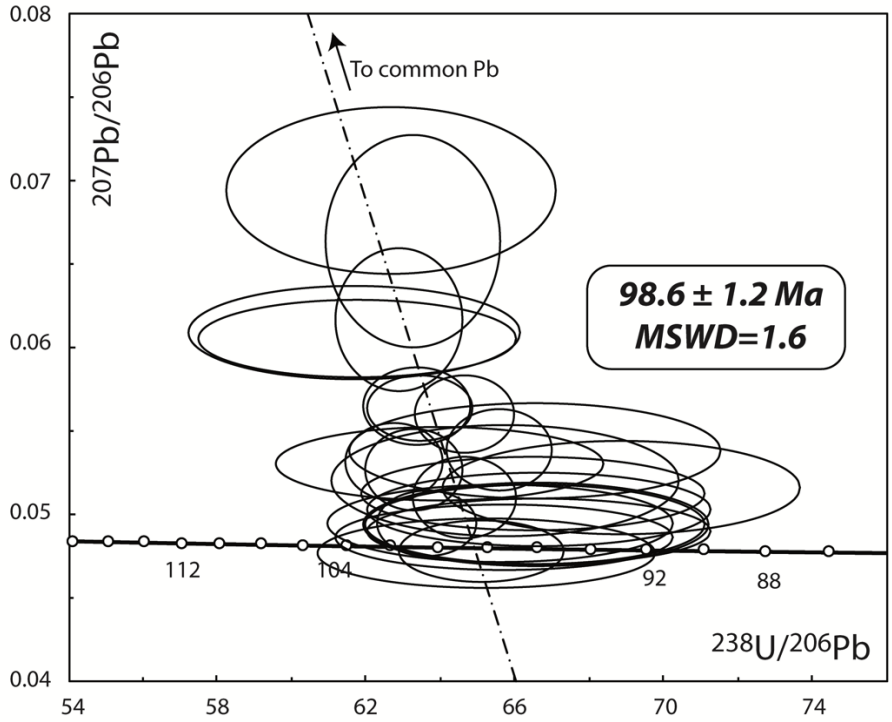

Figure 11: Diagramme Tera-Wasserburg des âges U-Pb des rutiles des échantillons BCOR 68a- b. Les ellipses d'erreurs représentent un intervalle de 2σ. L'intercept inférieur donne une date à 98,6 ± 1,2 Ma qui est également reportée avec une erreur de 2σ.

Table 6 : Analyses roches totales tirées de Monchoux (1972a). 1, 2, 3 : roches à saphirine dépourvues de calcite, collectées à une distance croissante du corps de Lherz. 4, 5: roches à saphirine avec calcite. *L.o.i.: Perte au feu.*

	1	2	3	4	5
SiO_2	45.30	42.70	37.90	23.00	23.60
Al_2O_3	15.30	16.30	19.10	9.40	11.10
Fe_2O_3	5.90	6.00	7.90	3.50	6.80
MgO	22.30	24.60	17.20	14.60	13.00
CaO	1.40	3.20	10.70	23.90	20.80
Na_2O	0.80	0.30	1.30	0.80	0.10
K_2O	0.08	0.10	0.80	0.04	0.00
CO_2	___	___	___	19.00	15.70
L.o.i	9.20	6.60	4.40	5.30	8.90
Total	100.28	99.80	99.30	99.54	100.00

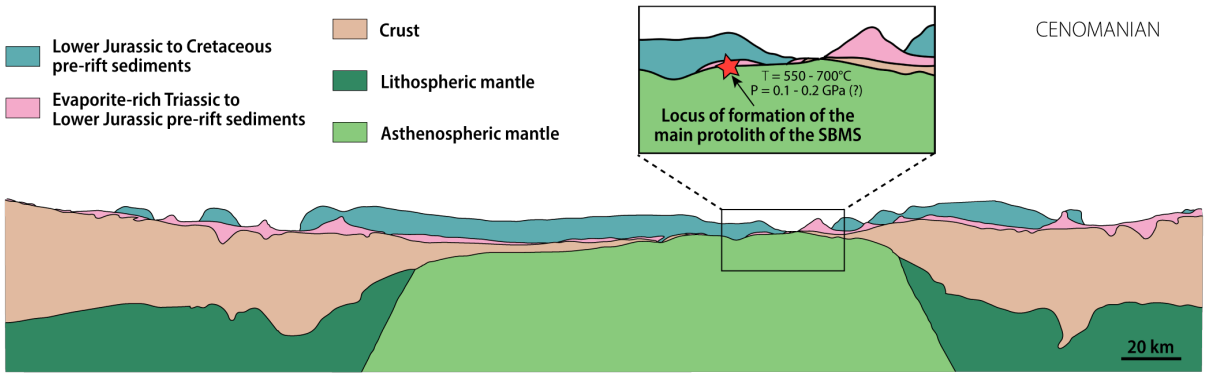

Figure 12 : Position du protolithe principal de l'assemblage minéralogique à saphirine au sein du rift pyrénéen déduite de cette étude (étoile rouge). La géométrie du rift est redessinée d'après Duretz *et al.* (2019). Les conditions P-T du métamorphisme du protolithe d'âge jurassique supérieur - triasique inférieur porté au contact du manteau asthénosphérique, déduites de cette étude, sont données avec leurs incertitudes dans la vue de détail de l'axe du rift.

1377